

AMERICAN UNIVERSITY OF BEIRUT

FLOW ASSESSMENT THROUGH IMAGING
TECHNIQUES: APPLICATIONS TO WIND
AUGMENTATION AND AORTIC
DISSECTION FLOW

by
ELIE SALAMEH

A thesis
submitted in partial fulfillment of the requirements
for the degree of Master of Engineering
to the Department of Mechanical Engineering
of the Faculty of Engineering and Architecture
at the American University of Beirut

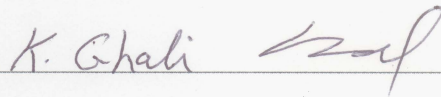
Beirut, Lebanon
July 2017

AMERICAN UNIVERSITY OF BEIRUT

FLOW ASSESSMENT THROUGH IMAGING
TECHNIQUES: APPLICATIONS TO WIND
AUGMENTATION AND AORTIC
DISSECTION FLOW

by
ELIE SALAMEH

Approved by:



Dr. Ghanem Oweis, Associate Professor
Mechanical Engineering

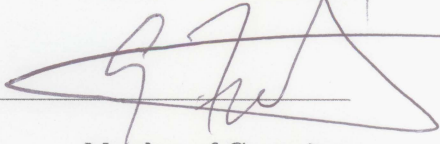
Advisor

Dr. Nesreene Ghaddar, Professor
Mechanical Engineering



Member of Committee

Dr. Ghassan Antar, Associate Professor
Department of Physics



Member of Committee

Date of thesis defense: July 27, 2017

AMERICAN UNIVERSITY OF BEIRUT

THESIS, DISSERTATION, PROJECT RELEASE FORM

Student Name: _____
Last First Middle

Master's Thesis Master's Project Doctoral Dissertation

I authorize the American University of Beirut to: (a) reproduce hard or electronic copies of my thesis, dissertation, or project; (b) include such copies in the archives and digital repositories of the University; and (c) make freely available such copies to third parties for research or educational purposes.

I authorize the American University of Beirut, to: (a) reproduce hard or electronic copies of it; (b) include such copies in the archives and digital repositories of the University; and (c) make freely available such copies to third parties for research or educational purposes after: **One ___ year from the date of submission of my thesis, dissertation or project.**
Two ___ years from the date of submission of my thesis , dissertation or project.
Three ___ years from the date of submission of my thesis , dissertation or project.

Signature

Date

This form is signed when submitting the thesis, dissertation, or project to the University Libraries

Acknowledgements

I would first like to thank my thesis advisor Dr. Ghanem Oweis from the Mechanical Engineering Department at AUB for his valuable assistance, patience, and support throughout the project duration. He consistently allowed this thesis to be my own work, but steered me in the right the direction whenever he thought I needed it.

I would also like to acknowledge Dr. Nesreene Ghaddar from the Mechanical Engineering department at AUB, and Dr. Ghassan Antar from the Physics Department at AUB as the committee members and second readers of this thesis, and I am gratefully indebted to their valuable comments and suggestions.

Special thanks go to Mr Joe Zullikian and Mr Joseph Nassif from the AUB machine shops who manufactured the models for both studies using CNC machining. Partial development of these studies took place as part the MECH 609 course given at AUB, and class discussions were helpful. I would like to extend my thanks to the university research board for its funding that allowed these studies to become possible.

Finally, I would like to express my gratitude to my parents and to my friends, especially that of my best friend and buddy Jaad Tannous, for providing me with unfailing support and continuous encouragement throughout my years of study and through the process of researching and writing this thesis. This accomplishment would not have been possible without them. Thank you.

Abstract

Elie Salameh for Master of Engineering
Major: Mechanical Engineering

Title: Flow Assessment Through Imaging Techniques: Applications to Wind Augmentation and Aortic Dissection Flow

Flow-Imaging techniques constitute an essential part in the field of experimental fluid dynamics due to their high-fidelity measurements of actual systems. Recent developments in these methods and their applications in the multiple aspects of aerodynamics, aeroacoustics, wind energy, and bio-inspired domains have led to numerous studies being performed and advancements being implemented. In this dissertation, established flow visualization methods Particle Image Velocimetry (PIV) and Laser-Induced Fluorescence (LIF) are employed to assess the fluid dynamics and flow structure of two selected applications, drawing from the wind energy and bio-inspired domains, in the aim of improving the understanding of the fundamental regimes governing them. In accordance, this thesis is composed of two parts presenting studies of each corresponding application. The first part handles the use of PIV to analyze the flow behavior and velocity augmentation inside several shroud geometries subject to free-stream conditions. To provide a reliable benchmark to flow augmentation coupled with the shrouding process and a data set for validation of CFD models, reduced-model geometries with different shroud variants are subjected to free-stream conditions inside a wind tunnel test section. PIV is then employed in order to measure the required velocity fields, allowing for extraction of the flow augmentation ratios and assessment of the shroud effect on the flow. The second part employs PIV and LIF in order to study the fluid dynamics inside an aortic dissection, a high-mortality cardiovascular disease. With the assistance of AUBMC radiologists, reduced aortic models with different disease configurations are placed in quasi-realistic conditions. PIV is then employed to generate a quantitative visualization of the flow dynamics, while LIF is used to extract specific flow patterns. LIF imaging, with its comparability with the CT-scanning machine used to diagnose dissections, provides radiologists with a reliable reference and helps to improve diagnostic accuracy.

Contents

Acknowledgements	iv
Abstract	v
1 Introduction	1
2 Flow Augmentation in Turbine-inspired Shrouds	3
2.1 Introduction	3
2.2 Aim of Research	6
2.3 Methods	7
2.4 Results	11
2.4.1 The Plain Duct:	11
2.4.2 Inclined Ducts:	16
2.4.3 Diffuser/Nozzle Geometries:	18
2.4.4 The Inlet/Outlet Flanged Configurations:	25
2.5 Summary and Conclusions	31
3 Flow Visualization in Aortic Dissections	33
3.1 Introduction	33
3.2 Aim of Research	37
3.3 Methods	38
3.3.1 Dissection Models and Flow Loop:	38
3.3.2 PIV and LIF Measurements:	41
3.4 Results	42
3.5 Summary and Conclusions	52
4 Conclusions	53

List of Figures

2.1	(<i>a</i>): Diffuser-Augmented Wind turbine (DAWT) coupled with a rear flange, as designed by [4]. (<i>b</i>): Flanged diffuser enclosure studied in [14].	5
2.2	Dimensioned Drawings along with their corresponding dimensional representations for the: (<i>a</i>): "Plain" geometry, (<i>b</i>): "Flanged" geometry, and (<i>c</i>): "Diffuser" geometry. All units in mm.	7
2.3	Experimental Setup schematic showing flanged duct model with corresponding PIV acquisition hardware	9
2.4	Velocity magnitude contours for the straight duct plain geometry for: (<i>a</i>): 15Hz Tunnel Frequency, and (<i>b</i>): 30Hz Tunnel frequency. All contours normalized by corresponding U_∞	13
2.5	Cross-sectional velocity cuts for the straight duct plain geometry for: (<i>a</i>): 15Hz frequency, and (<i>b</i>): 30Hz frequency. The red lines represent the locations of the duct walls.	14
2.6	Streamwise sections through the duct CL for the plain and incline duct cases. All units normalized.	15
2.7	Velocity Magnitude contours for the inclined duct cases for: (<i>a</i>): 10° incline, (<i>b</i>): 20° incline, and (<i>c</i>): 30° incline. The purple lines depict the location of the duct centerline.	17
2.8	Velocity magnitude contours for the diffuser configurations for the: (<i>a</i>): 15Hz frequency, (<i>b</i>): 30Hz frequency. All units are normalized.	20
2.9	Velocity magnitude contours for the nozzle configurations for the: (<i>a</i>): 15Hz frequency, (<i>b</i>): 30Hz frequency.	21
2.10	Streamwise section linear plots for: (<i>a</i>): Diffuser 15Hz, (<i>b</i>): Diffuser 30Hz.	22
2.11	Streamwise section linear plots for: (<i>a</i>): Nozzle 15Hz, (<i>b</i>): Nozzle 30Hz.	23
2.12	C_P field for the Diffuser Duct 15Hz configuration	24
2.13	C_P field for the Nozzle 15Hz configuration	24
2.14	Diffuser and Nozzle configurations studied in [4]. The ratio l/W utilized for these cases is equal to 7.7.	25

2.15	Velocity magnitude contours for the "Flanged" duct geometry in the outlet flange configuration for: (a): Outlet Flange 15Hz and (b): Outlet Flange 30Hz.	27
2.16	Velocity magnitude contours for the "Flanged" duct geometry in the inlet flange configuration for: (a): Inlet Flange 15Hz and (b): Inlet Flange 30Hz.	28
2.17	Streamwise velocity magnitude sections for the "Flanged" duct geometry in the inlet flange configuration for: (a): Inlet Flange 15Hz and (b): Inlet Flange 30Hz.	29
3.1	Most common aortic dissection type classification as presented in [57]	34
3.2	(left) Schematic of the AD flow loop and the laser diagnostic system for PIV and LIF; (right) a picture of an AD model installed in the test setup	38
3.3	(a) Dimensioned drawings of the two machined AD models. The channel is 14 mm deep. (b) Eight test cases are investigated with the red arrow symbolizing flow direction. (E) is designated for entry-tear cases, and (R) for reentry tear cases. There are four cases with entry tear flap (left) and four with reentry tear flap (right). Each flow geometry is labeled.	40
3.4	Velocity magnitude contours for (a) the four models with entry flap, and (b) the four models with the re-entry flap. Color scale is in mm/sec.	44
3.5	Flow velocity magnitude in the true (black) and false (gray) lumens for (a) the four models with entry flap, and (b) the four models with the re-entry flap. Plot order follows that in fig. 3.4	46
3.6	(a) Instantaneous LIF images showing the shear layer in an entry-reentry AD; (b) the penetration of the entry flow into the stagnant false lumen blood.	46
3.7	Instantaneous LIF images of the dye bolus flow front for (a) the four AD cases with entry flap, and (b) the four cases with the re-entry flap. The time stamp corresponds to the plots in fig. 3.9.	48
3.8	Spatially-averaged LIF time trace signal for AD case B2-F (a): uncorrected; and (b): linearly-corrected for light sheet intensity variations.	49
3.9	Spatially-averaged and intensity-corrected LIF time trace signals for six AD cases: (a): A2-F, (b): B1-F, (c): B2-F, (d): A2-R, (e): B1-R, (f): B2-R. Red lines are time stamps corresponding to figs. 3.6, 3.7	51

List of Tables

- 2.1 Blockage areas and corresponding ratios for the different employed geometries in comparison with the wind tunnel test section 11
- 2.2 Augmentation table for all 13 cases discussed in the result section. U_∞ taken from plain cases to avoid larger stagnation effects present in other cases. 30

Abbreviations

PIV	Particle-Image Velocimetry
LIF	Laser-Induced Fluorescence
CFD	Computational Fluid Dynamics
AD	Aortic Dissection
HAWT	Horizontal-Axis Wind Turbines
VAWT	Vertical-Axis Wind Turbines
CCD	Charge-Coupled Device
FOV	Field of View
CL	Centerline
TTE	Trans-Thoracic Echocardiography
TEE	Trans-Esophageal Echocardiography
CT	Cardiac Computed Tomography
MRI	Magnetic-Resonance Imaging

Chapter 1

Introduction

The creation and development of flow-imaging techniques throughout the recent years has paved the way for an improved understanding of complex flow models [1]. Because of their close comparability with actual systems due to accurate flow behavior capture [2], [3], flow models assessed with these imaging techniques present a high degree of fidelity and can serve as reliable benchmarks in comparisons with potential flow theory and CFD models. With applications in the multiple aspects of aerodynamics, aeroacoustics, wind energy, and bio-inspired domains, these methods have established themselves as essential cogs in the experimental fluid dynamics field. In this dissertation, established flow visualization methods such as Particle Image Velocimetry (PIV) and Laser-Induced Fluorescence (LIF) are employed to assess the fluid dynamics and flow structure of two selected applications, drawing from the wind energy and bio-inspired domains, in the aim of improving the understanding of the fundamental regimes governing them.

The first part handles the use of PIV, along with available potential flow theory models, to analyze the flow behavior and velocity augmentation inside of several shroud geometries subject to free-stream conditions. This study bases on the current research being performed on wind energy devices as part of the optimization initiative in the renewable energy domain, as well as the wind flow around buildings, and is inspired by ducted wind turbines. Reduced model geometries with different shroud variants are subjected to free-stream conditions inside of a wind tunnel test section. The PIV setup allows the captured data to measure the velocity field, which allows the calculation of the velocity augmentations and subsequent static pressure coefficient (C_P) gradients around and inside each respective shroud. These parameters are used as a basis to further promote scientific knowledge regarding flow augmentation in shrouding geometries in a free-stream and form a basis for the selection of the optimal geometry and configuration in the design of ducted wind turbines, supplementing and improving on the study performed in [4].

The second part employs PIV and LIF in order to study the fluid dynamics inside an aortic dissection, a high-mortality cardiovascular disease. Aortic dissections, located in the aortic artery, are tears that typically develop between the inner walls of the aorta and allow blood to flow between these layers, forming another conduit, denoted as a false lumen [5]. Two main types of aortic dissections exist, relating to the location of development of the tears, with the ascending aorta type being the more life-threatening [6],[7]. In order to diagnose this phenomenon, Contrast Computer Tomography (CT) scanning is employed. CT scanning utilizes a reactive contrast media fluid, injected into the patient that allows the machine to visualize the flow as the fluid circulates inside the aorta [8],[9],[10]. Despite this method being well-established, rates of false diagnosis remain significantly high [11],[12], and in accordance with the bio-inspired research process and based on the request of radiologists from the AUBMC, a better understanding of the hemodynamics inside the aortic arch is required to assist in improving diagnostic accuracy. For this purpose, reduced aortic arch models with several dissection configurations are designed and subjected to conditions similar to the ones found inside an actual aorta. Two imaging techniques, PIV and LIF, are then utilized to assess the flow. PIV is employed and allow to generate a quantitative model on the behavior of the flow throughout the different lumens, while LIF is used as the main imaging technique due to its comparability with the CT scanner used on actual dissections. LIF allows the visualization of flow development, vortex shedding, as well as residency time calculation through the manipulation of the corresponding luminosity fields. These results are compared with an actual CT scan of the model in order to locate similarities and allow radiologists to more accurately diagnose aortic dissections.

Chapter 2

Flow Augmentation in Turbine-inspired Shrouds

2.1 Introduction

The wind energy sector has witnessed a steady growth rate during the last few years, with the globally-installed energy capacity increasing from 159GW by the end of 2009 to 194GW by 2010 [13], and reaching a 30% annual growth by 2013 [14]. With Horizontal-Axis wind turbines (HAWTs) forming the bulk of wind-energy harvesting devices due to their simple design, improved performance parameters, as well as an established foundation [15], [16], initiatives to increase their corresponding energy output production, in terms of both raw mechanical power and aerodynamic efficiency, have spanned various forms depending on the required power output scale and the type of energy-conversion equipment [17], [18], [19]. In terms of maximizing aerodynamic efficiency, a significant amount of technical work has been conducted, chiefly through the optimization of turbine blade design in order to minimize stall and wake effects, as presented in [20], [21], and [22]. On large scale devices, researchers have investigated the optimal spatial arrangement of turbines in wind farms to minimize wake losses [23], [24]. Wind-speed augmentation has also been an essential criterion for optimizing energy production and maximizing efficiency, especially as the output wind power scales cubically with speed (V^3), as shown in eq. 2.1, with k being a coefficient of performance; i.e. a 26% augmentation in wind speed would yield up to a 100% power increase. Several aspects of wind augmentation have been implemented, although large-scale devices rely primarily on passive flow acceleration types, focusing on the appropriate site selection. In order to select the optimal wind farm locations, Meteorological data were consulted over extended periods of time and geographies, and stable and maintainable target speeds were selected, with the selection criteria presented in [25], [26], [27], and [28].

$$P = \frac{1}{2}\rho kAV^3 \quad (2.1)$$

For smaller scale wind turbines, such as those intended for urban environments to supplement the power grid or provide energy for individual appliances and residential units, the form of wind augmentation is more dependent on the wind turbine type, differentiating between horizontal-axis or vertical-axis wind turbines (VAWTs). Multiple studies on VAWT optimization have been conducted, with their corresponding augmentation methods classified into either uni- or omnidirectional wind inlets, with each category varying in complexity and potential benefits [29]. However, as VAWTs are significantly less employed than horizontal-axis devices as they require an external energy source for blade-rotation initialization, possess lower wind-power extraction efficiencies, and present several design limitations due to their support locations [16], the main focus remains on HAWTs and their corresponding optimization methods.

Smaller-scale HAWTs require more active augmentation techniques in addition to the passive site-selection criteria. With this scale of turbines being common to urban environments, wind speed augmentation strategies for HAWTs require sufficient understanding of the complex wind flow patterns around buildings for optimal placement of wind turbines on roofs and around structures, as discussed in [30], [31], [32], [33], [34], and [35]. One particularly interesting modification implemented on these turbines was the installation of a duct or shroud around the rotor blades, which allows for a more active form of augmentation. Shrouding was found to be particularly cost-effective for smaller-scale turbine rotors typical of urban settings [36]. Shrouding was noticed not to be restricted to wind energy applications [37], but was also commonly employed in a multitude of other applications, namely in propeller systems [38], axial flow pumps [39], marine propellers [40], marine energy extractors [41], as well as in aerodynamic propulsion [42]. Among the numerous recent studies conducted, diffuser-shaped shrouds were observed to have the most efficient flow augmentation ratios, as first presented by [43], and further studied by [44], [45], [46], [47], [48], and [49]. These shrouds were constructed to be short in length, with the turbine blades placed at the duct inlet, typically at the front. In addition to the shrouding process, recent studies performed by [14] and [4] demonstrated that adding a rear flange to the duct would contribute to further lowering the back-pressure at the turbine exit and thus induce an additional flow acceleration in-duct, such as the shroud configurations shown in fig. 2.1.

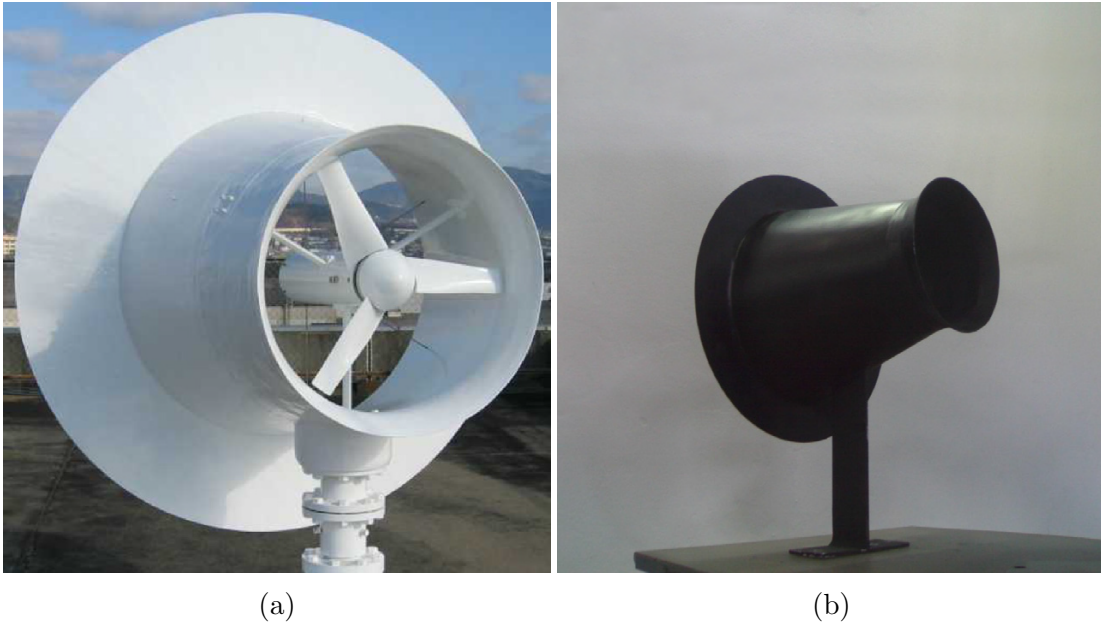


Figure 2.1: (a): Diffuser-Augmented Wind turbine (DAWT) coupled with a rear flange, as designed by [4]. (b): Flanged diffuser enclosure studied in [14].

While the configurations presented in the literature did indeed demonstrate a significant augmentation factor to both velocity and power generation, the study in [4] presented a more comprehensive approach to the shroud geometry selection criteria for wind turbine power augmentation. In accordance, the current study aims to draw from the results obtained in [4] and provide a more generalized shrouding selection methodology.

2.2 Aim of Research

This dissertation part aims to provide experimental insight into wind augmentation inside an empty duct along the free-stream by varying its external shape. As based on potential flow theory, the external duct geometry provides an essential factor in setting the pressure field outside the duct. As in a one-way coupled flow, the pressure difference across the length of the duct between the inlet and the outlet drives the duct flow. Multiple validations of this observation have been conducted as potential flow computations by a number of researchers to assess the flow acceleration in a duct and gain basic physical insight [48], [50], while more complicated numerical methods have been employed for complex flow patterns unresolvable by inviscid theory [51] and [52]. In accordance, the interior geometry and internal dimensions of the ducts are fixed to provide a baseline for case-by-case comparison.

Viscous effects such as vorticity generation at boundaries have been found to cause significant deviations from inviscid predictions, especially in experimental flow investigations. Additionally, increasing the length of the duct contributed to significantly reducing the cross-talk flow between its inlet and outlet. From an empirical view, recent implementations on ducted wind turbines seem to gravitate towards very short ducts to enhance this type of flow. In the current study however, this effect is maintained to a minimum by designing ducts with an increased length-to-width ratio l/W of 3. This parameter allows for the minimization of the cross-talk effect as well as the reduction of vorticity generation in the vicinity of the duct interior, increasing the comparability with inviscid flow studies and with the results obtained from [4]. In addition, while the presence of a rotor within or in the vicinity of the duct may indeed significantly modify the flow patterns and introduce variable dynamics, the flow behavior in the studied hollow geometries is of a fundamental importance in terms of flow feature assessment, and provides a baseline for the design of the optimal turbine shroud and possible rotor placement for a maximized potential augmentation factor.

2.3 Methods

Three main reduced-model geometries representing the most commonly-employed and applicable enclosures are constructed using 4mm -thick clear-cast acrylic sheets, glued together using clear Cyanoacrylate adhesive for optical access to the inside flow of the duct. The model edges are then covered with reactive Rhodamine B dye to allow for proper edge visualization and prevent reflections. All models have a fixed $30\text{mm} \times 30\text{mm}$ internal cross-section. Although a circular cross-section may provide a closer estimate to the actual turbine enclosure flow, a square area is utilized in order to facilitate flow visualization and prevent issues encountered with circular areas, as discussed in [53], and mentioned in [2] and [3]. In addition, the conditions of the testing environment may provide reliable comparability between both geometries as the tested parameters depend on a planar model configuration and attempt to minimize three-dimensional effects. Dimensioned drawings of the geometries are presented in fig. 2.2.

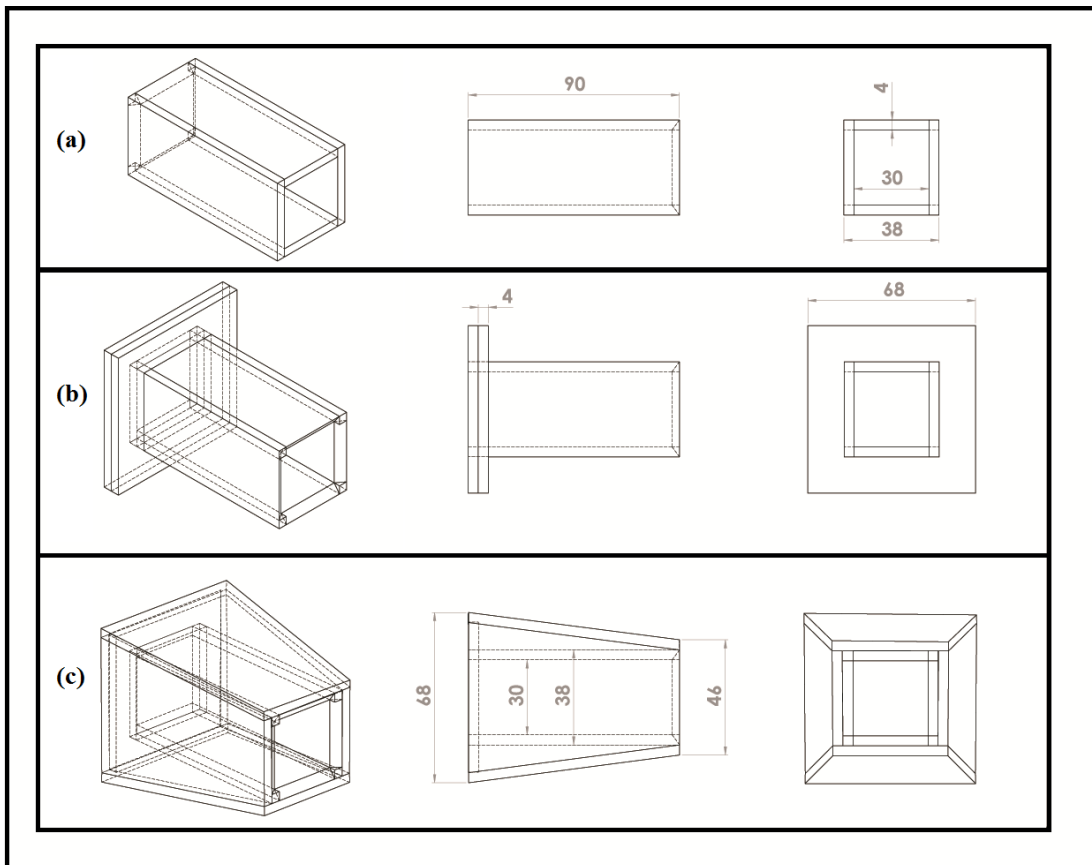


Figure 2.2: Dimensioned Drawings along with their corresponding dimensional representations for the: (a): "Plain" geometry, (b): "Flanged" geometry, and (c): "Diffuser" geometry. All units in mm.

The outer geometries are varied in order to produce several testing configurations, with all models subjected to free-stream conditions inside an open-loop wind tunnel test section. The L-shaped wind tunnel incorporates a 90cm -long test section, with a square cross-section of $45\text{cm} \times 45\text{cm}$. The inlet and outlet are open to space and are situated far enough from walls to avoid disturbing the flow. An exit blower driven by a 25-hp variable frequency drive motor generates the flow, and can achieve speeds in excess of 50 m/s in the test section (Engineering Laboratory Design, MN, USA). The streamwise turbulence intensity in the empty test section is obtained from previously-measured data and found to be around 0.5% [54]. The section is constructed from 1in. -thick clear-cast acrylic sheets that provide ample optical access to the flow for imaging diagnostics and model setup. Particle Image Velocimetry (PIV) is employed as the main imaging technique as it provides reliable quantitative measurements that allow the measurement of the velocity flow fields within and around the enclosure geometries. Velocity data are acquired at two nominal free-stream speeds: 12 m/s and 24 m/s, corresponding to preset frequencies on the drive motor dial (15Hz and 30Hz respectively). These values are chosen in accordance with standard wind turbine operating Reynolds numbers of $Re = 24000$ and $Re = 48000$, corresponding to each wind speed respectively, calculated based on the duct internal width W .

Each duct test model is placed at the approximate center of the tunnels test section by screwing it onto a $20\text{cm} \times 2\text{cm} \times 1\text{cm}$ elliptical cross-section rigid arm fixed from one end to a side wall of the wind tunnel. The duct is aligned with the free-stream wind direction. A schematic of the basic experimental setup is shown in fig. 2.3.

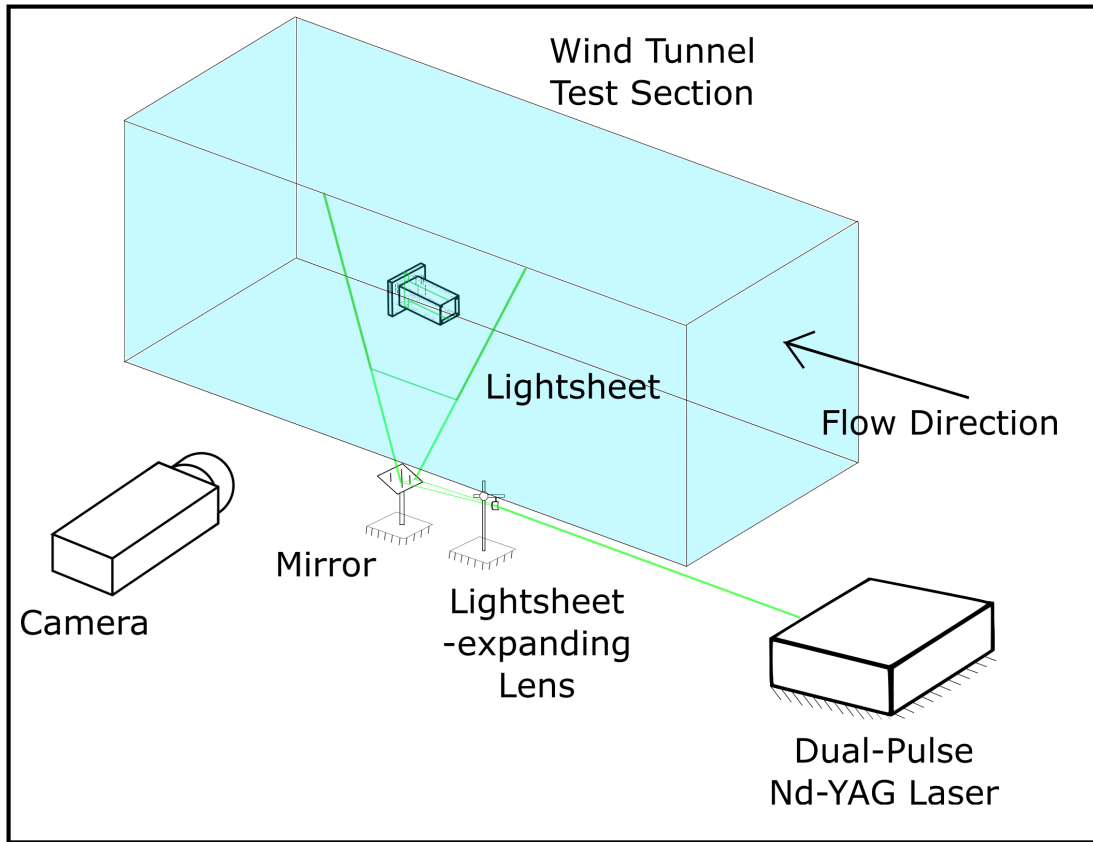


Figure 2.3: Experimental Setup schematic showing flanged duct model with corresponding PIV acquisition hardware

The plain geometry, as shown in fig. 2.2a, maintains a constant outer cross-sectional area along the wind direction. This case is employed as a benchmark and reference for the other configurations. In addition, this geometry is tested with its axis tilted to the free-stream at three angles, testing at one wind tunnel frequency (15Hz) for reference purposes, in order to assess stall behavior and mimic changes in wind direction. The axis is tilted at 10 deg, 20 deg, and 30 deg to model effects similar to the low wind-speed turbine performances observed in the literature. The diffuser-geometry depicted in fig. 2.2b is split into two configurations, based on the sign of the outer area slope with the flow direction. In the case where the slope is positive, meaning the area increases with the flow, it is denoted as a "Diffuser" case, while for the configuration where the slope is negative, or the area is decreasing, the "Nozzle" case naming is assigned. The last two configurations, referring to the geometry shown in fig. 2.2c, include an external flange mounted at one end of a straight duct, denoted as "Inlet Flange" or "Outlet Flange" models depending on the flange location along the flow. These multiple configurations amount to a total of 13 studied cases, further widening the span of the assessed shrouding effects.

A $1mm$ -thick laser lightsheet is introduced from the bottom wall of the test section for flow visualization, which illuminates a vertical plane aligned with the free-stream wind direction, passing through the center-plane of the duct. A dual-head Nd-YAG Laser (Quantel, France) with a $8ns$ pulse duration, $120mJ/pulse$ energy output, and a $532nm$ wavelength is employed as the main illumination source. The $1\mu m$ smoke particles generated by atomizing olive oil using a six-jet atomizer (TSI, USA) are used as flow tracers. The smoke is introduced through the wind tunnel bell-shaped meshed inlet in order to allow full mixing and to minimize flow disturbance in the test section. The laser light reflected by the smoke particles is recorded using a high-speed double-shutter cross-correlation CCD camera (Sensicam SVGA, PCO, Germany). The camera is additionally fitted with a $0.5nm$ optical-notch filter that eliminates background wavelengths and prevents over-saturation. The $1280px \times 1024px$ camera is aligned perpendicular to the lightsheet, and images an approximate field of view of $155mm \times 125mm$ to visualize the wind flow patterns within the duct model and in its immediate vicinity. The chosen FOV is taken based on the calibration between the largest possible view field and the optimal camera resolving power for the smoke particles. Approximately 500 particle-image pairs are taken for each test case at a maximum acquisition rate of 4Hz, while the inter-frame PIV time delay is taken at $70\mu s$ and $35\mu s$, corresponding to the 15Hz and 30Hz frequency cases accordingly. The image pairs are analyzed with the PIVLAB 2000 cross-correlation code in Matlab environment [55] using a final window size of $32px \times 32px$ with multi-pass PIV processing. The percentage of vector outliers obtained is typically less than 2%, with these vectors removed using median filtering and scatter-plot elimination. The mean of all the instantaneous velocity vector fields is computed for each case in order to produce the time-averaged velocity fields used in augmentation assessment and comparison. In addition, the static pressure coefficient C_P can be generated by applying the Bernoulli assumption to the existing flow. As the increased l/W prevents cross-talk and reduces viscous and vorticity effects inside the duct, as studied in [4], the coefficient C_P can be formulated through eq. 2.2. This allows for the calculation of pressure coefficient fields for the corresponding velocity magnitudes U in each case. The dimensionless ratio C_P allows the visualization of possible low-pressure suction regions related to velocity augmentation, paving way for an increased understanding of the required geometry features for an optimal shroud design.

$$C_P = \frac{P - P_\infty}{\frac{1}{2}\rho U_\infty^2} = 1 - \frac{U^2}{U_\infty^2} \quad (2.2)$$

2.4 Results

With the duct length-to-width ratio l/W maintained at 3, typically longer than what has been recently used in ducted wind turbines [4], [36], [44], [46], [49], the cross talk between the inlet and outlet is minimized, allowing the visualization of the isolated effect of the enclosure geometry on the wind flow augmentation passing through the duct interior, as well as the approximation of the static pressure coefficient C_P .

Another factor required in assessing the augmentation effect is the wind tunnel blockage ratio [4]. The blockage ratio is calculated for all configurations as well as for the rigid connector arm by comparing the total test section cross-sectional area with their corresponding section footprints, as shown in table 2.1. This ratio is found to within the 2% range for all cases, which is well below the 10% limit proposed by [56] for wind tunnel blockage effects. From a mass conservation point of view, one would expect flow augmentation to be proportional to the blockage ratio; however, as the blockage ratios are almost negligible, this augmentation can thus be attributed to a more local effect, demonstrated by the viscous effects and wake formations relating to the change in duct geometries in each corresponding case.

Designation	Effective Area (cm^2)	Blockage Ratio
Wind Tunnel	2025	—
Connector Arm	40.00	1.9753%
Straight Duct	5.440	0.2686%
Flanged Duct	35.89	1.7723%
Diffuser Geometry	35.89	1.7723%
Inclined Duct 10deg	8.933	0.4411%
Inclined Duct 20deg	25.27	1.2477%
Inclined Duct 30deg	29.61	1.4620%

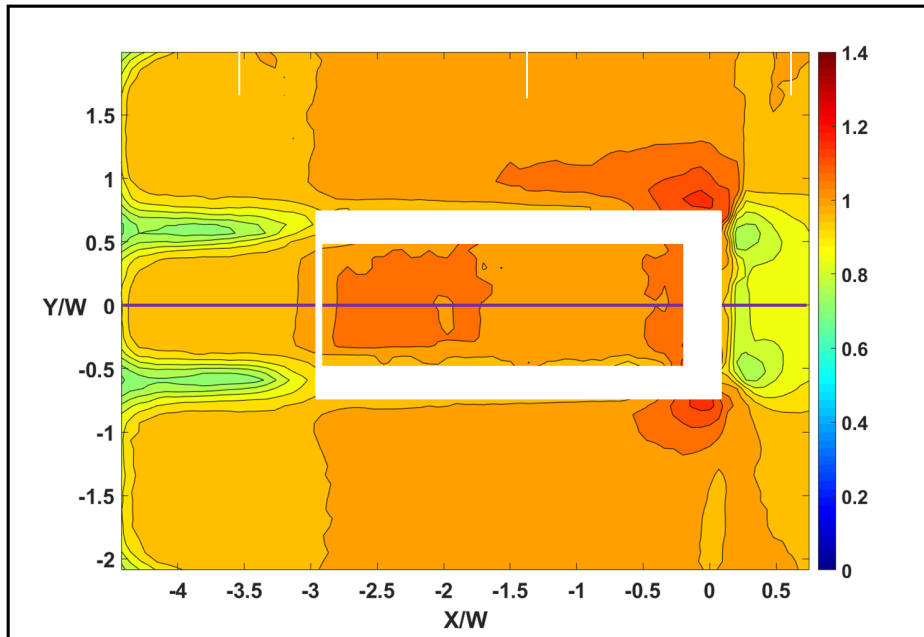
Table 2.1: Blockage areas and corresponding ratios for the different employed geometries in comparison with the wind tunnel test section

2.4.1 The Plain Duct:

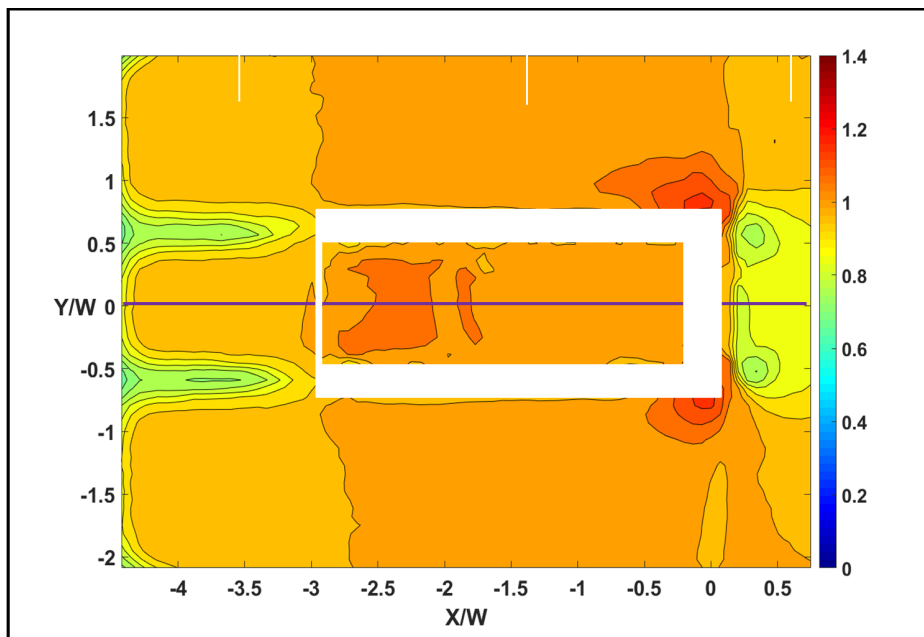
The velocity magnitude contours for the plain model configuration measured using PIV are normalized by the corresponding free-stream velocities and are presented in fig. 2.4 for the two tested cases of Re . The white regions represent the duct geometry locations while the three white lines on the top side of fig. 2.4a represent the locations of the vertical velocity sections extracted from the same fields. These sections are utilized in order to visualize the flow development

throughout the different stages of its motion and offer a comparison criterion for flow augmentation assessment across the different cases. The zero location is taken at the duct direct inlet for all cases. The free-stream velocities U_∞ associated with the normalization process are taken by obtaining the mean of the velocities of four vectors on both the top-right and bottom-right corners of the studied PIV window. This allows for the calculation of an approximate incoming free-stream velocity for each case, independent of the geometry and as far as possible from the duct walls in order to avoid the stagnation effect. These velocities can also be employed in validation with the wind tunnel input frequencies utilized. All axis scales are normalized by scaling them with the corresponding duct width W , where $X = x/W$ and $Y = y/W$. The x -axis origin is taken at the inlet position, while the y -axis origin is taken with respect the location of the centerline of the duct, improving visualization of the flow symmetry and extraction of the streamwise velocity profiles for each case.

It can be noticed from fig. 2.4 that slight augmentation is present inside the duct region, defined as increase in average internal mass flow of around 4-5%, which is an order of magnitude larger than the area blockage ratio (0.2%). In the external region of the duct, especially in the area directly upstream of the inlet, a uniform flow deceleration of about 15% is noticed. This velocity decrease is also clearly seen in the cross-sectional velocity cuts, presented in fig. 2.5. The coordinate representations in this case are related to the normalized motion along and perpendicular to the duct centerline. While in the plain duct cases, these coordinates: x and y are equal to the previously-defined X and Y , this designation is particularly useful when dealing with the inclined duct cases.

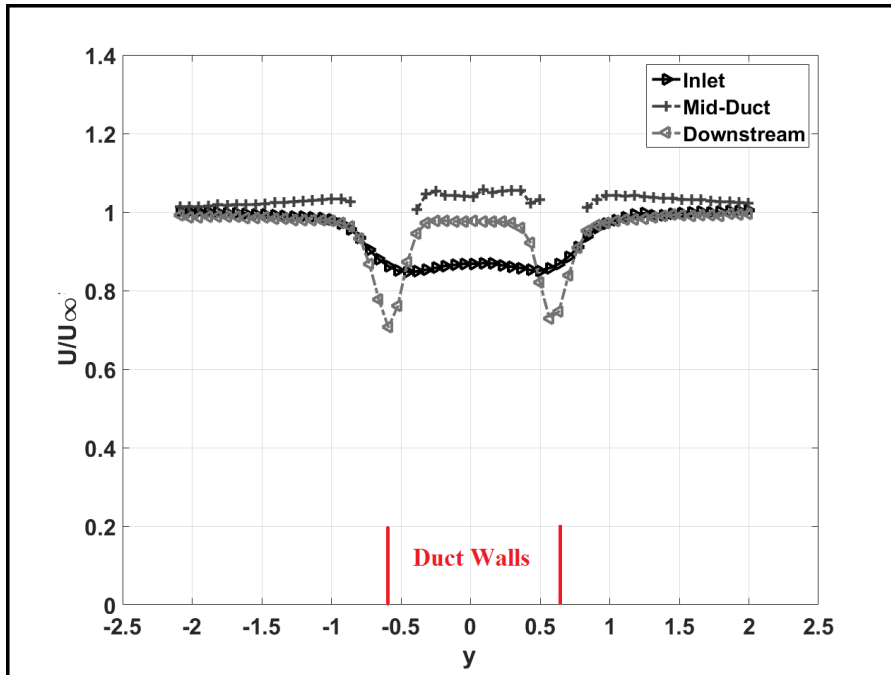


(a)

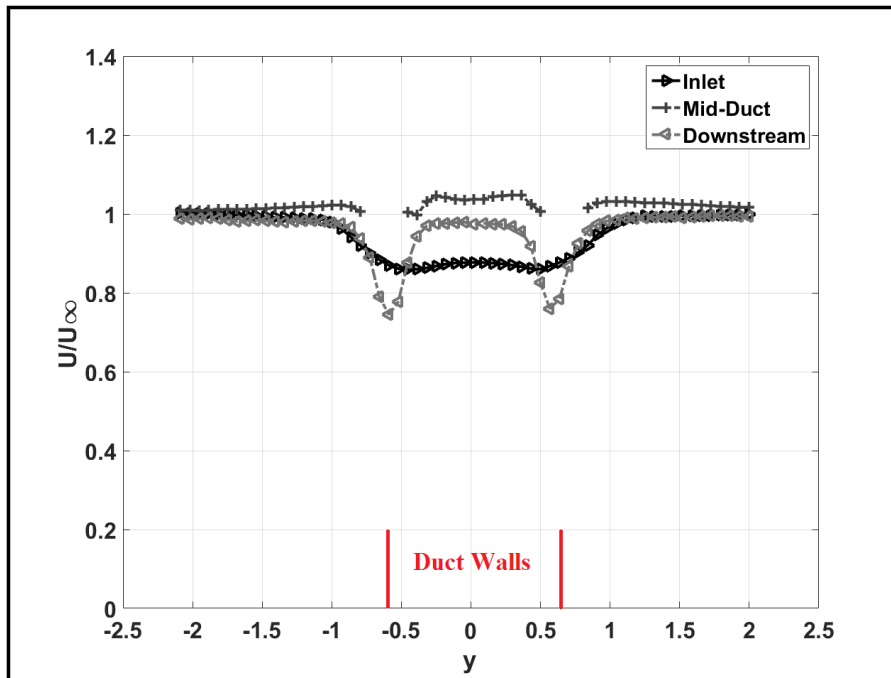


(b)

Figure 2.4: Velocity magnitude contours for the straight duct plain geometry for: (a): 15Hz Tunnel Frequency, and (b): 30Hz Tunnel frequency. All contours normalized by corresponding U_∞



(a)



(b)

Figure 2.5: Cross-sectional velocity cuts for the straight duct plain geometry for: (a): 15Hz frequency, and (b): 30Hz frequency. The red lines represent the locations of the duct walls.

The stagnation effect experienced is most likely due to incoming upstream flow seeing the entire duct, including its open internal area, as a stoppage block. The regions just around the frontal corners of the duct witness flow acceleration, under the same effect, extending approximately a half-duct length, $W/2$, in the downstream direction. Additionally, the wake behind the duct walls manifests clearly just downstream of the duct end, as seen by the dips in the velocity profiles in fig. 2.5. The flow pattern with respect to the duct centerline is noted to be approximately symmetric.

The streamwise velocity magnitude linear plots along the duct centerline provide an improved particle-tracing technique. As shown in fig. 2.6, these sections demonstrate that a fluid particle decelerates from the free stream speed U_∞ to approximately 85% U_∞ just at the duct front, while inside the duct it speeds up to 105% and upon exiting the duct, drops back to around 95% U_∞ . This allows for a visualization of the more local effect of shrouding on flow augmentation, and, with the increase duct length-to-width ratio, provides insight on the limiting length condition required for optimal results.

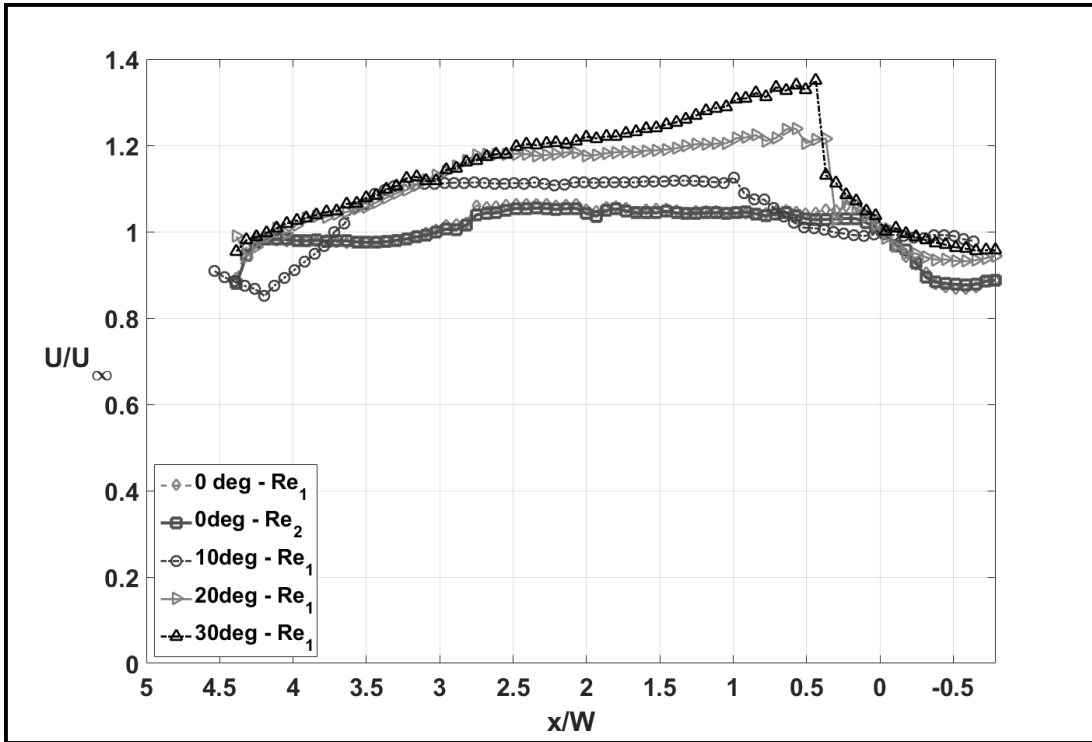
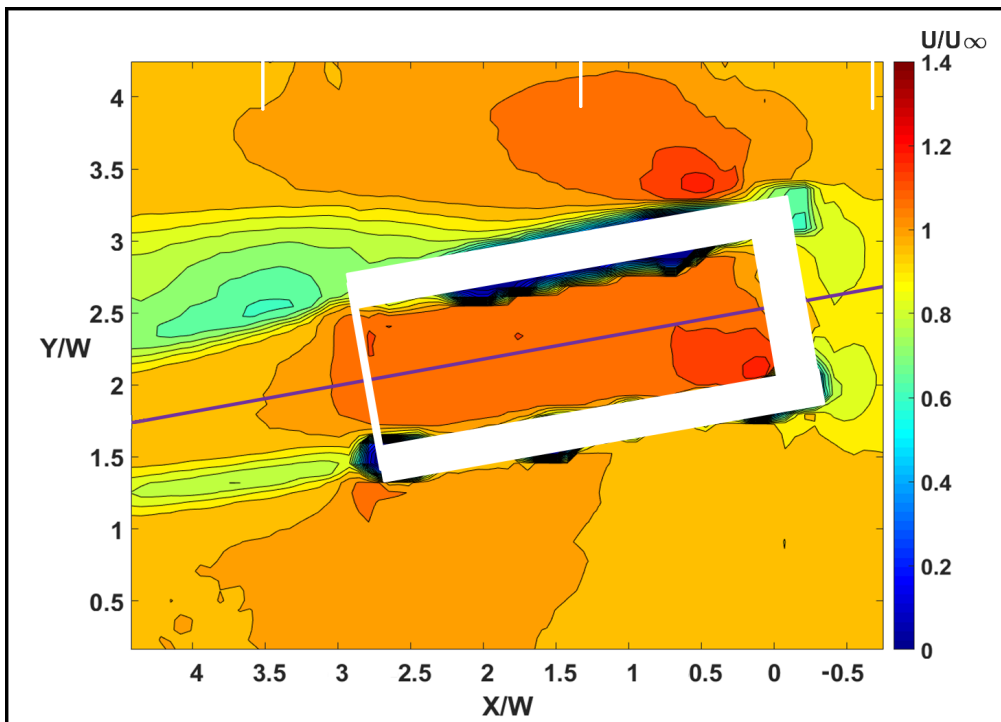


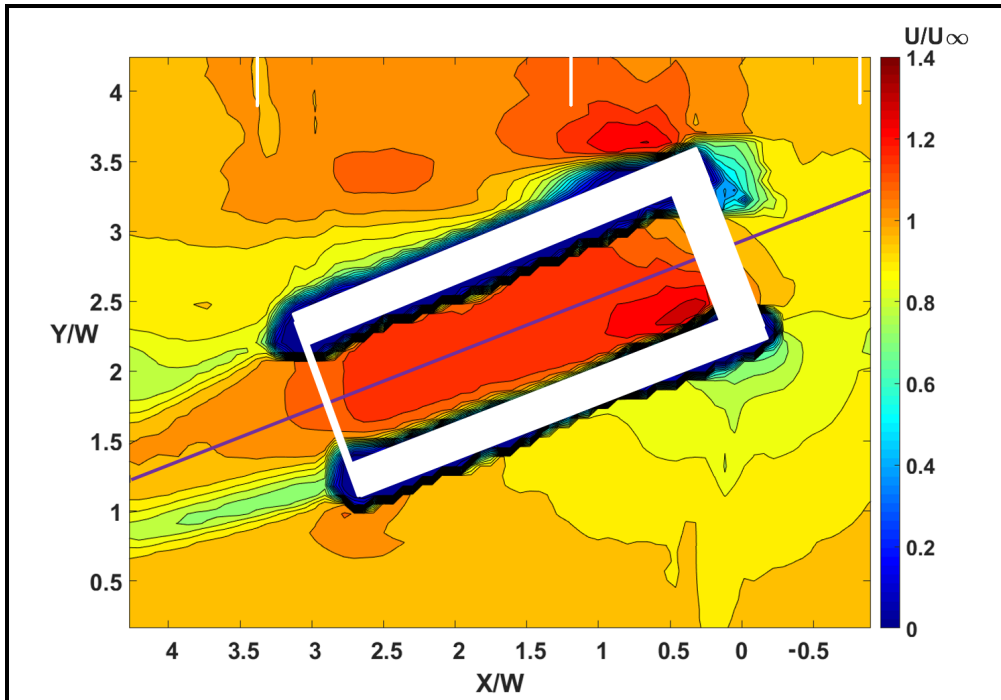
Figure 2.6: Streamwise sections through the duct CL for the plain and incline duct cases. All units normalized.

2.4.2 Inclined Ducts:

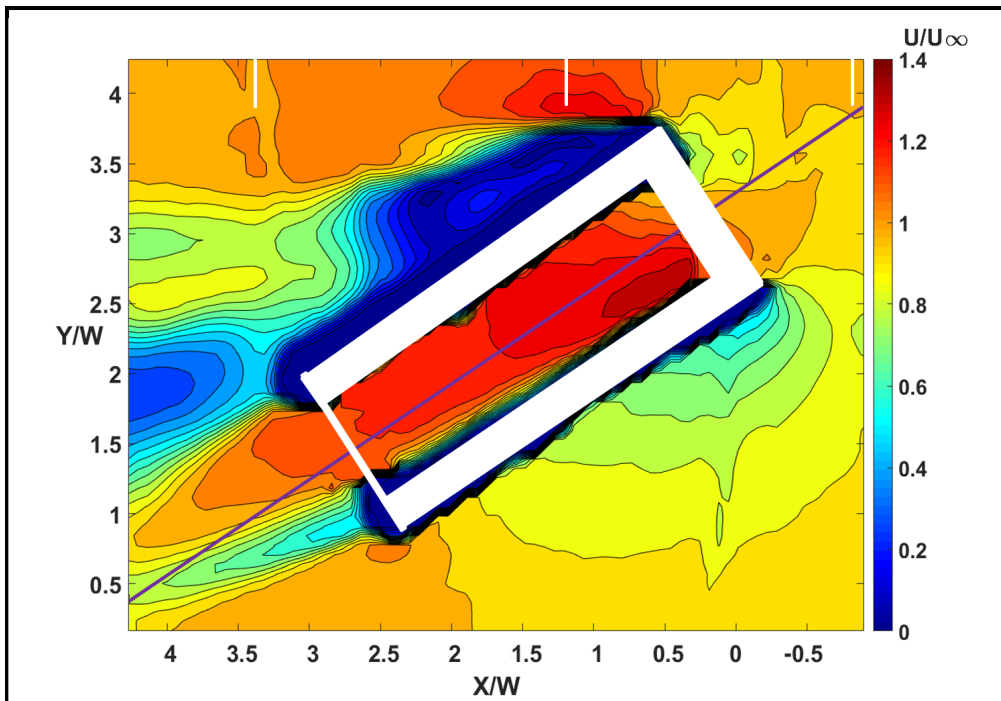
As the wind direction may vary with the turbine, a sample case is chosen in order to study the effect of this directional shift on a turbine enclosure. As a basis to this study, the plain duct enclosure is rotated along the flow at three standardized angles. When the ducts centerline is inclined relative to the incoming flow direction, the flow becomes non-symmetrical above and below the centerline, both internally and externally. This level of non-symmetry increases with increasing angle, and can be seen in the velocity magnitude contours corresponding to the inclined duct cases in fig. 2.7.



(a)



(b)



(c)

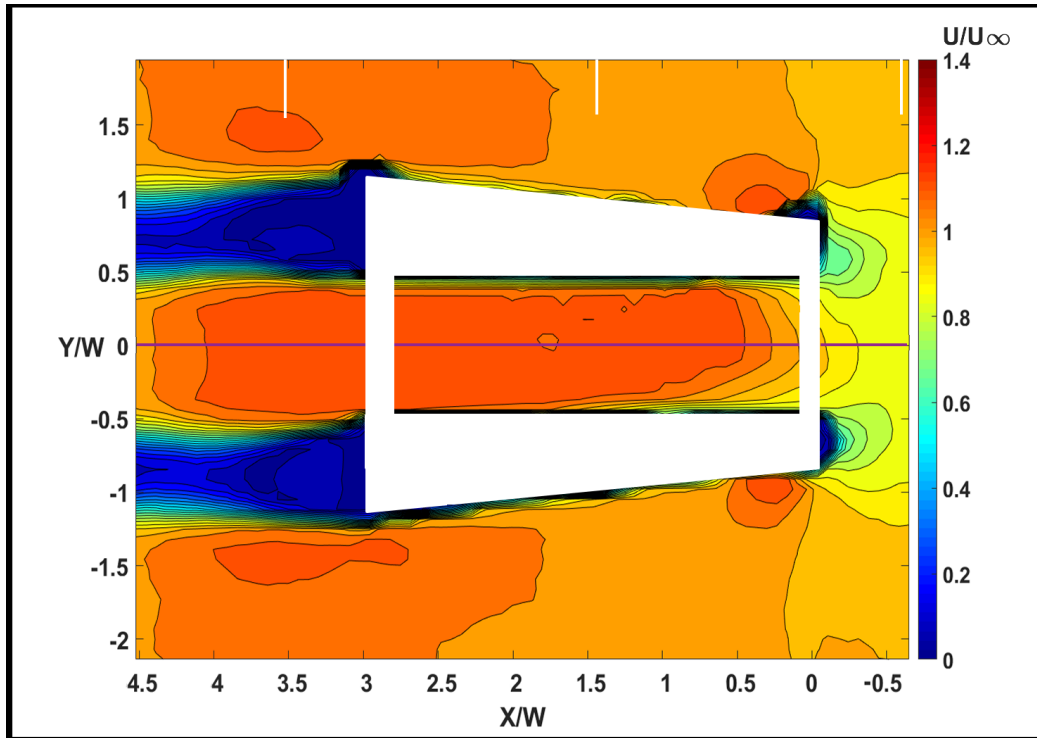
Figure 2.7: Velocity Magnitude contours for the inclined duct cases for: (a): 10° incline, (b): 20° incline, and (c): 30° incline. The purple lines depict the location of the duct centerline.

The average in-duct augmentation ratios are calculated to be approximately 10%, 17%, and 20% for the 10°, 20°, and 30° inclinations respectively. However, the center-line velocities can locally exceed these values, as shown in fig. 2.6. In the region external to the duct, similarly to the plain duct cases, the contours exhibit velocity deceleration as the flow encounters the duct frontal area. However, as the inclined cases possess a larger blockage ratio, the stagnation effects shift, where deceleration occurs along the underside of the duct's external bottom wall while a corresponding acceleration is witnessed along the duct top. Adjacent to the upper wall of the duct, and right downstream of the front corner, flow deceleration associated with the development of a separation bubble is noticed, the extent of which reaches the downstream end of the duct and connects with the wake from the duct top wall. All these effects produce somewhat of a funneling effect into the duct interior through the generation of back pressure, accentuating with increasing inclination angle.

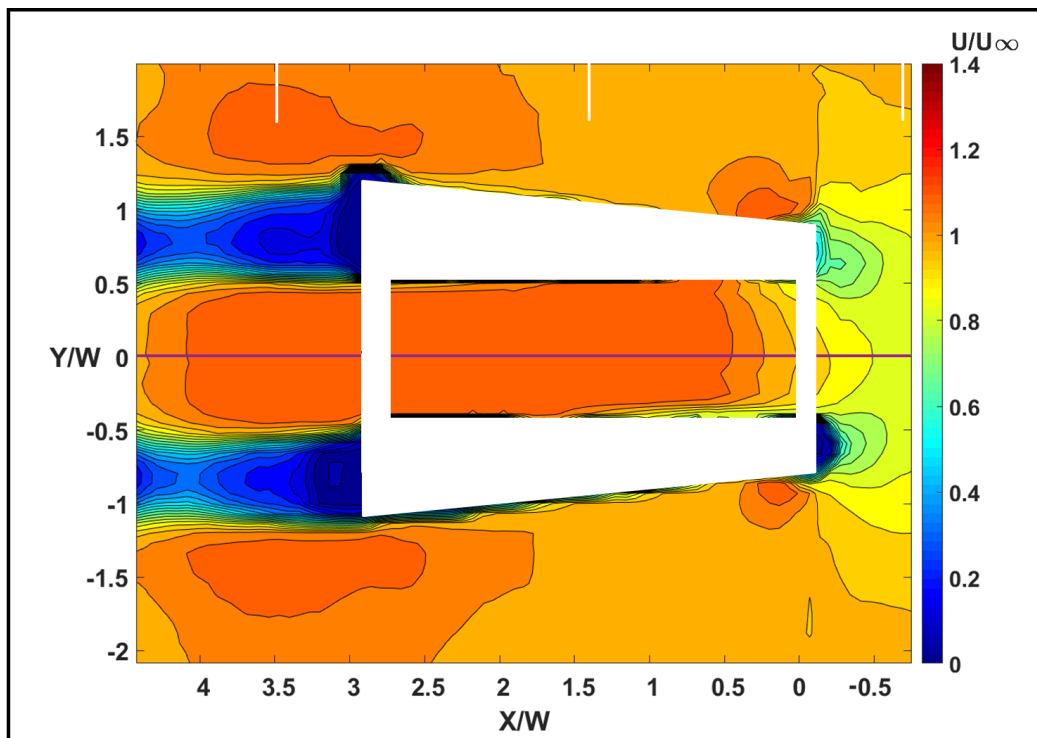
2.4.3 Diffuser/Nozzle Geometries:

These cases are characterized by the "Diffuser" geometry type, as in fig. 2.2b. The velocity magnitude contours for both the diffuser and nozzle cases are measured using PIV and are depicted in figs. 2.8 and 2.9. From an inviscid, potential flow viewpoint, the external flow acceleration in the downstream direction for the diffuser cases would be expected to lead to a reduction in the pressure, such that a favorable pressure gradient is generated to augment the flow inside the duct, in reference to the potential flow model generated in [48]. The average flow augmentation in the duct interior is calculated to be approximately 12% for both Re values. When the model is tested in the diffuser configuration, an externally-adverse pressure gradient would be expected, as deduced through the potential flow model, which would produce higher mass flowrates through the duct interior than in the nozzle configuration. However, the PIV measurements seem to contradict this claim, and in fact the 14% superior average flow augmentation in the nozzle configuration as compared to the diffuser case suggests that the external flow dynamics are more complex than is expected from inviscid arguments. The velocity contours depict a significantly larger shear layer, or wake, coming off the frontal face of the nozzle model, extending to the end of the duct and connecting with the downstream wake. This wake introduces an additional effective flow blockage not seen in the diffuser model, where no separation bubble is noticeable due to the difference in geometry alignment with the flow. This effective blockage deflects and accelerates the external flow significantly, with the acceleration extending well outside the field of view. This may be causing a reduction in the static pressure downstream to create a net favorable pressure gradient inside the duct. Hence, the flow deviates significantly from inviscid expectations due to the highly viscous effects associated with the formation of shear layers. The stream-

wise velocity sections for both configurations further enforce this observation, and provide additional insight on the local nature of the resulting augmentation, as shown in figs. 2.10 and 2.11. While the diffuser cases exhibit a more uniform augmentation profile, nozzle cases display a more localized higher augmentation peak towards the duct inlet, which may give some insight into the relation between the nature of the wake and the resulting performance boost. The static pressure coefficient field for the diffuser and nozzle configurations is calculated by applying eq. 2.2 to the corresponding velocity magnitude fields. The C_P fields for these cases allow the visualization of the low-pressure regions responsible for this suction effect. The obtained fields for the 15Hz frequency case are shown in figs. 2.12 and 2.13 for simple comparison. From these figures, it can be deduced that the desirable C_P values inside the duct lie in the negative range, corresponding to the suction effect, while values closer to 1 symbolize stagnation. Although these fields are similar in consistency to their corresponding velocity magnitude values, the C_P fields show a clear shift in low-pressure region locations. The diffuser case in fig 2.12 shows a negative region towards the rear of the duct, where the wake effects are mostly produced. However, the nozzle in fig. 2.13 demonstrates a frontal negative region that extends more over the duct length.

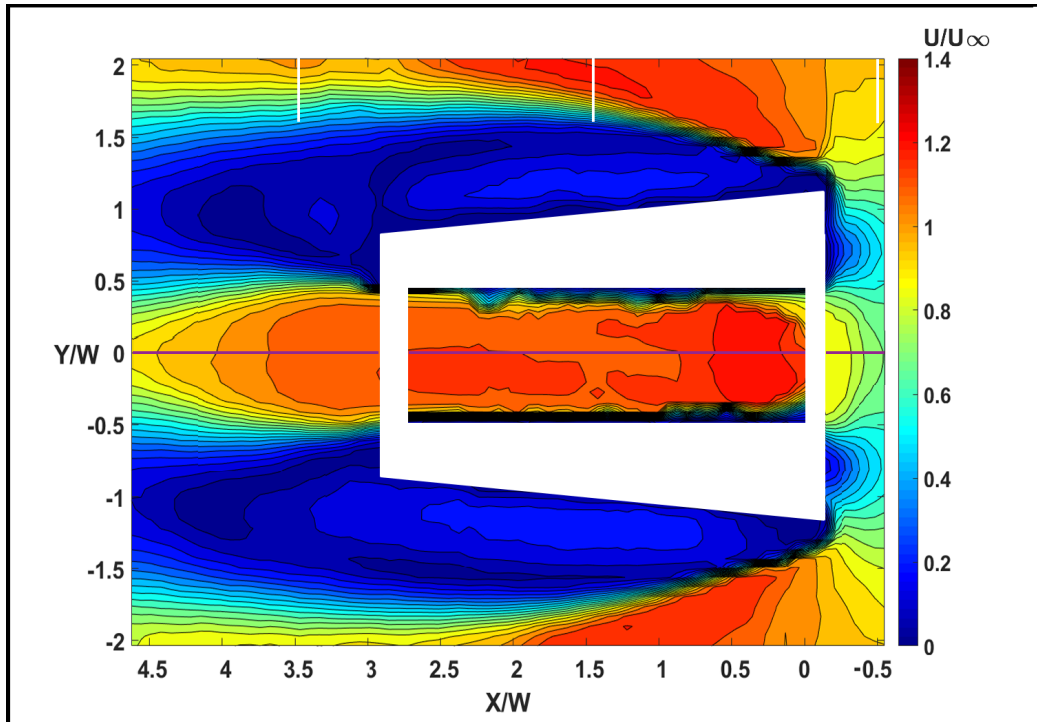


(a)

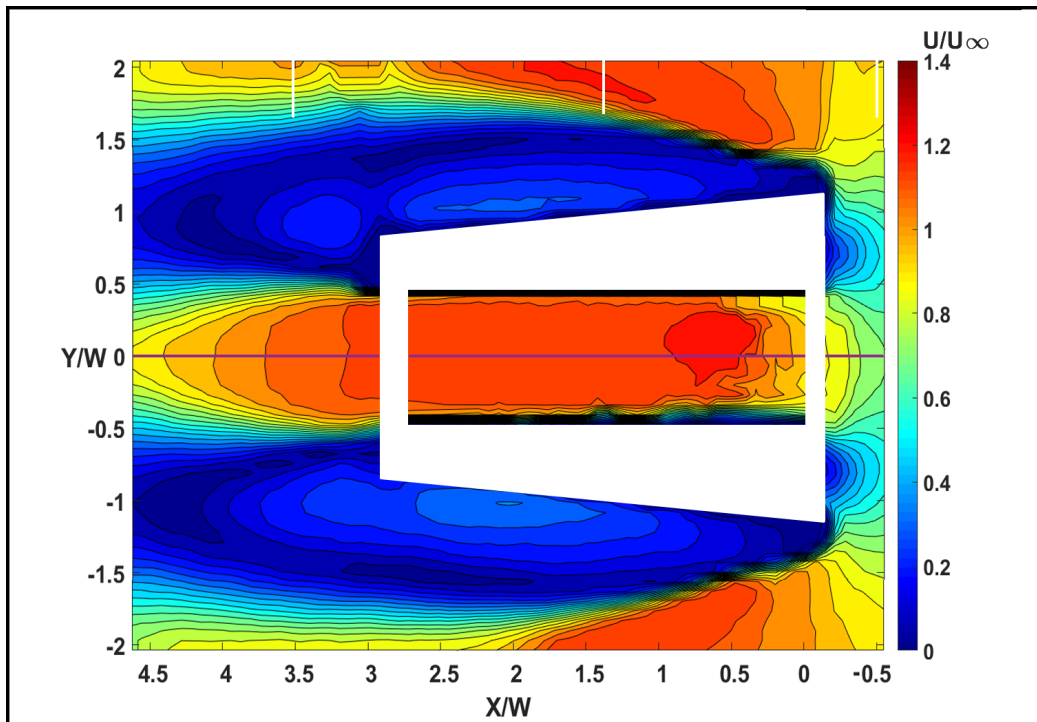


(b)

Figure 2.8: Velocity magnitude contours for the diffuser configurations for the: (a): 15Hz frequency, (b): 30Hz frequency. All units are normalized.

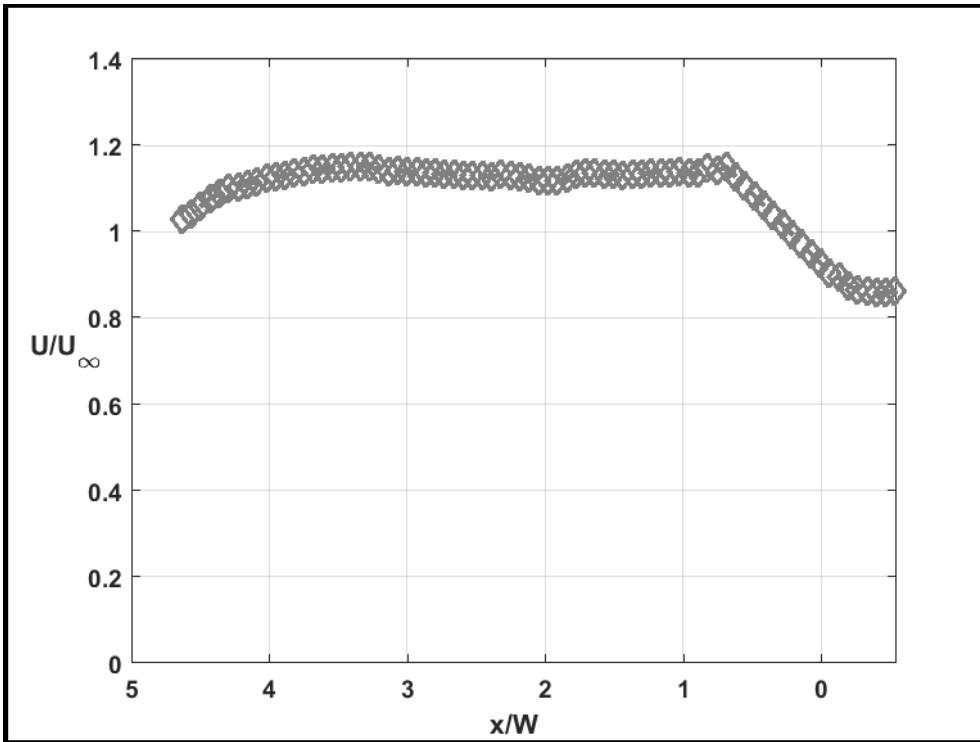


(a)

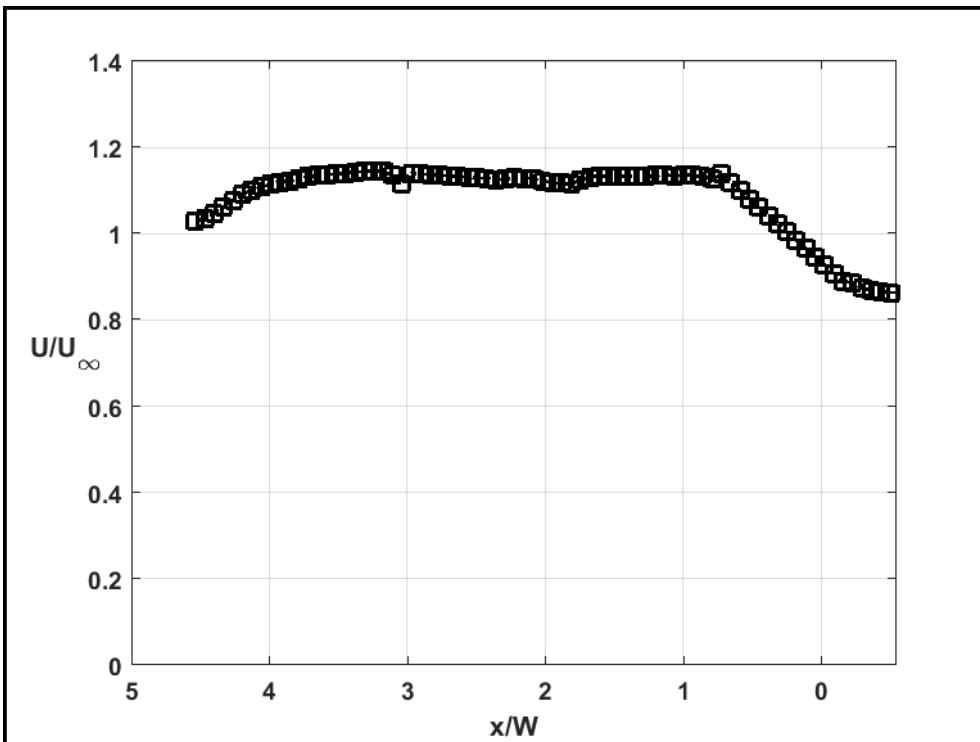


(b)

Figure 2.9: Velocity magnitude contours for the nozzle configurations for the: (a): 15Hz frequency, (b): 30Hz frequency.

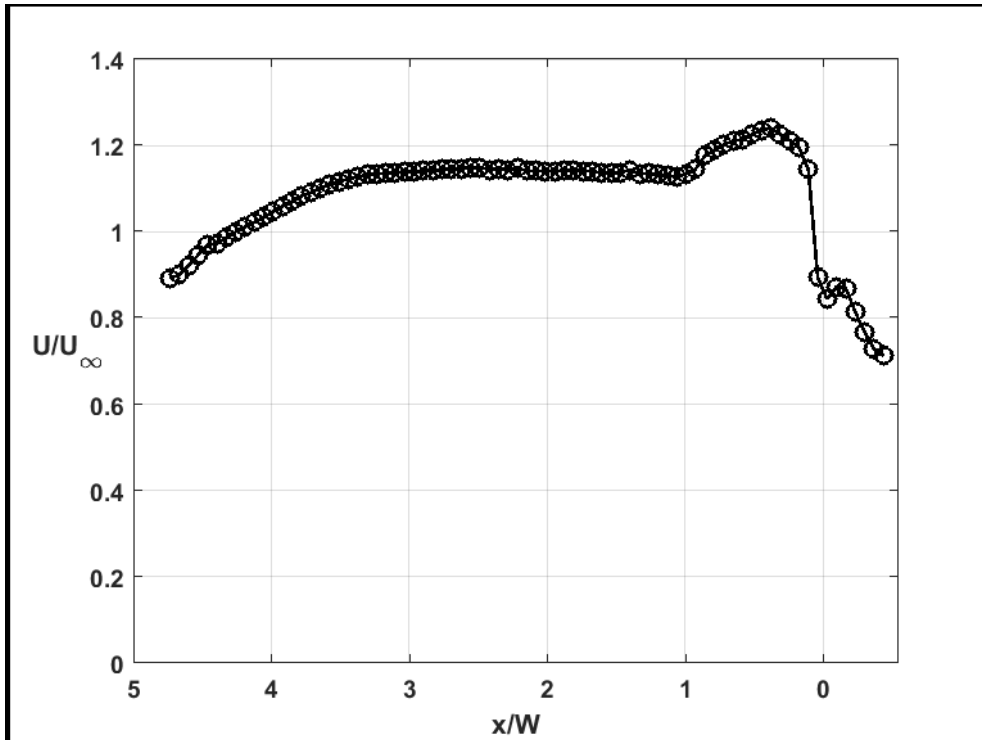


(a)

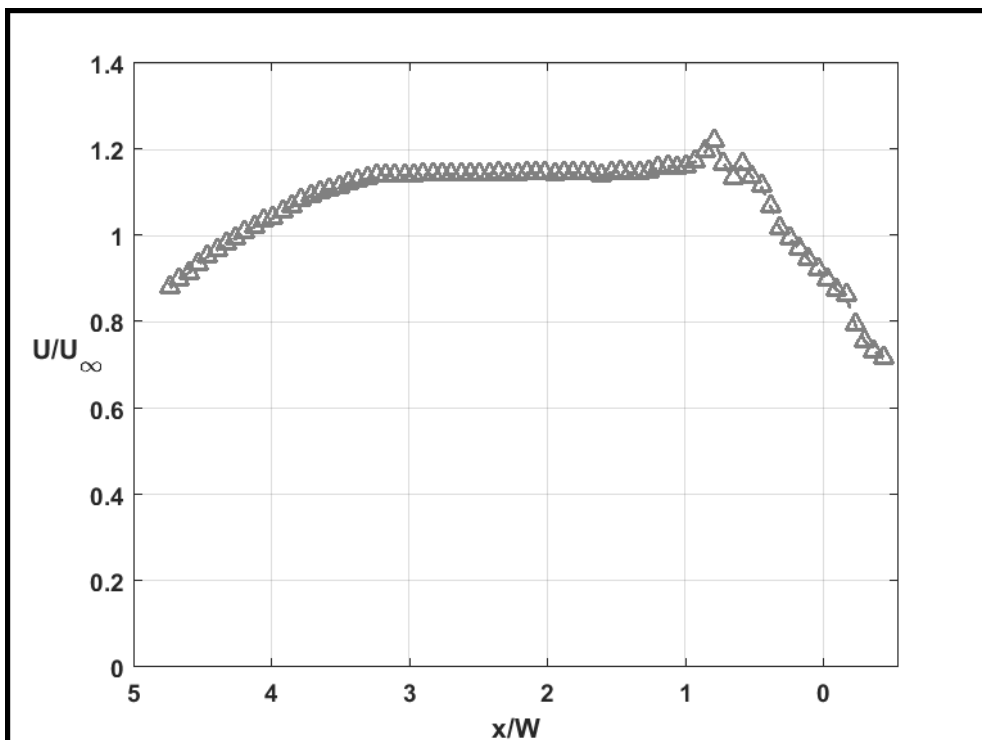


(b)

Figure 2.10: Streamwise section linear plots for: (a): Diffuser 15Hz, (b): Diffuser 30Hz.



(a)



(b)

Figure 2.11: Streamwise section linear plots for: (a): Nozzle 15Hz, (b):Nozzle 30Hz.

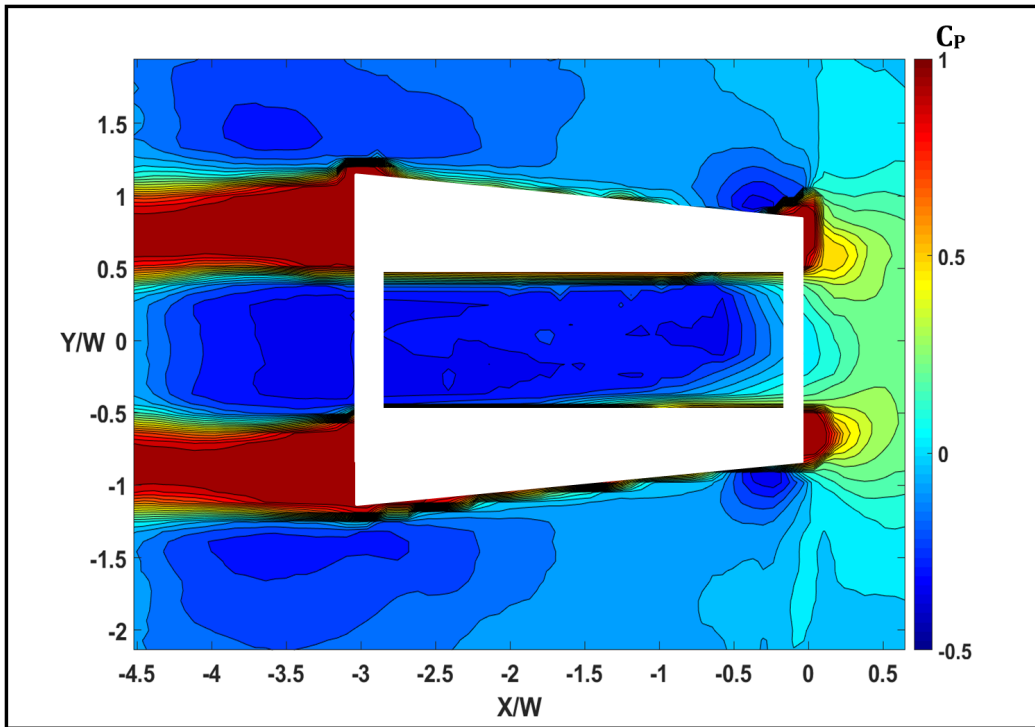


Figure 2.12: C_P field for the Diffuser Duct 15Hz configuration

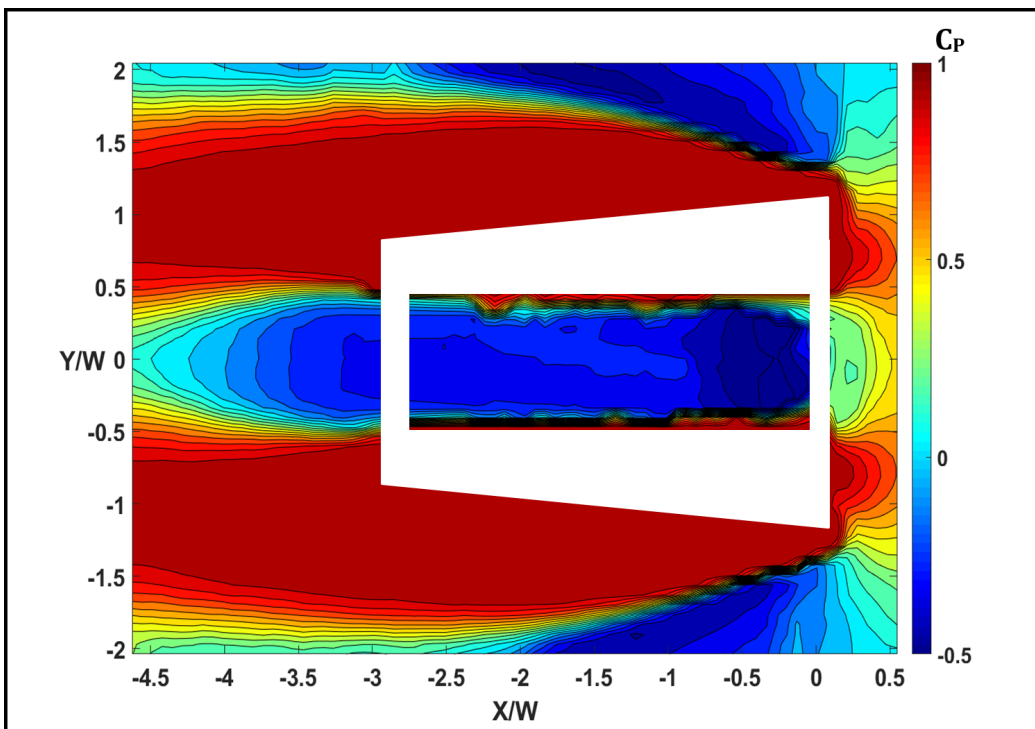


Figure 2.13: C_P field for the Nozzle 15Hz configuration

In reference to [4] that provided a wind tunnel visual analysis for both diffuser and nozzle geometries, as shown in fig. 2.14, the corresponding cases studied here exhibit smoother velocity profiles inside the ducts, as shown in the streamwise sections in figs. 2.10 and 2.11, most likely due to their constant internal area. Furthermore, this constant area causes the nozzle front to represent a larger obstacle for incoming flow, possibly contributing to a higher augmentation. However, it should be noted that with the presence of highly viscous effects around the ducts, the application of C_P in terms of the Bernoulli assumption might not be valid. Still, these fields do provide some insight on the location of the augmentation origin in tandem with the wake distribution.

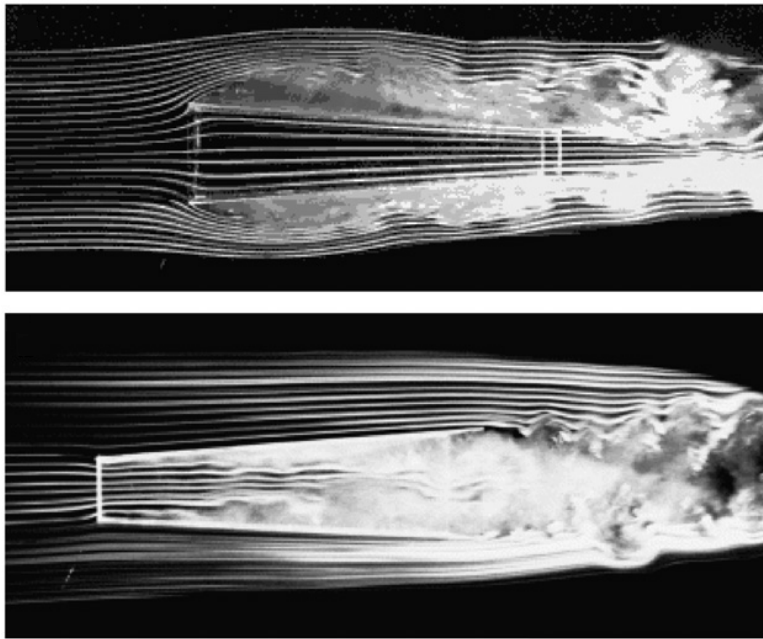


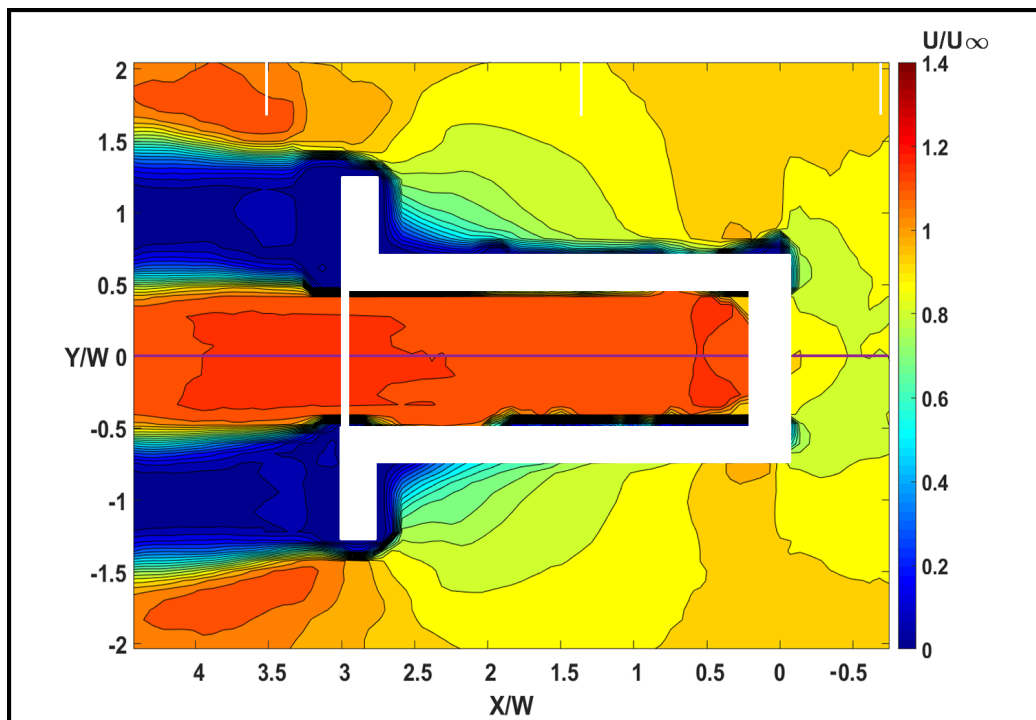
Figure 2.14: Diffuser and Nozzle configurations studied in [4]. The ratio l/W utilized for these cases is equal to 7.7.

2.4.4 The Inlet/Outlet Flanged Configurations:

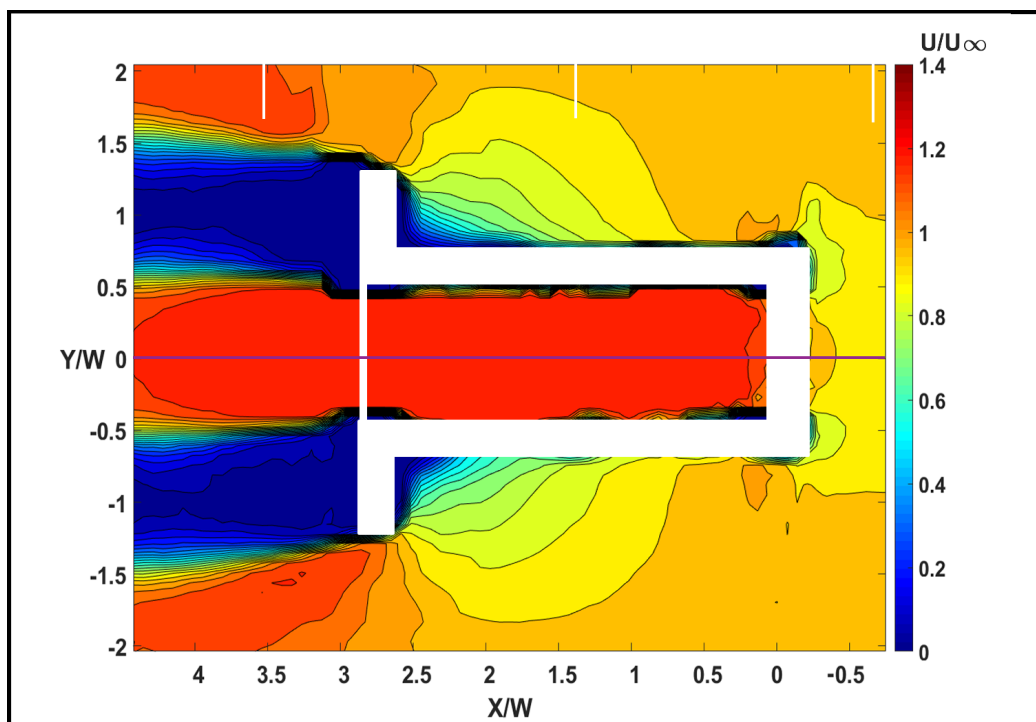
The flanged configurations consist of adding a flange to the plain duct case, as shown in fig. 2.2c. The location of the flange is then shifted by rotating the model 180degree . This allows for the creation of two main cases, denoted as "Inlet" and "Outlet" flanges. Similar to the diffuser geometry cases, the flange installed on the plain duct contributes to the generation of a significant wake. The highly-viscous effects are even more dominant in the area behind the outlet flange models, as shown in the corresponding velocity magnitude contours in fig. 2.15. Duct flow augmentation in these cases display significant dependence on Reynolds number, where the augmentation increases from 13% to 20% between the low and high Re cases. For both Re , there is significant flow deceleration

directly upstream of the duct inlet, leading to an increase in static pressure that assists pushing the flow inside the duct. The clear difference in the flow patterns between the two Re cases can be noticed in a more compact-sized deceleration region but larger deceleration for the higher Re case upstream of the duct inlet which is expected to induce higher static pressure and higher flow augmentation through the duct. The wake patterns downstream from the outlet possess similar characteristics for the two Reynolds numbers, and are limited in extent to the region right downstream of the flanges. The flow pattern for the inlet flange model case is quite different however. Similar to the nozzle model flow, which exhibits a very large wake coming off its front face, the inlet flange case exhibits a large wake behind the flange that extends well beyond the downstream end of the duct, as shown in the velocity magnitude contours (fig. 2.16) and the streamwise linear plots (fig. 2.17) for the inlet flanged cases. This large wake region forces the external flow to deviate out of the viewing plane, similar to the nozzle cases. However, unlike these cases, the inlet flange average flow augmentation inside the duct for the two Re cases is calculated at around 20%, a significant increase as compared to the nozzle's 14% boost. This observation allows the generation of an improved insight on the nature of the wake. The position of the flange is important to generate a forward-induced wake as well as a spanning one that contributes to a higher suction effect as result of the flow deviation, forcing the remaining flow inside the duct and creating this augmentation. It can thus be deduced that the effective frontal blockage area is the main augmentation driver. This can be further validated from the inclined cases that create an increasing funnel effect with increased angle, hence an increased blocking ratio. However, this should not be mistaken for the wind tunnel blockage ratio, as all values do not exceed the 2% mark, as shown in table 2.1, and thus pertains to a more local effect.

In order to simplify visualization of the calculated augmentation ratios for each case, the calculated results are compiled in table 2.2, allowing the selection of the possible optimal configuration for employment in turbine shroud design.

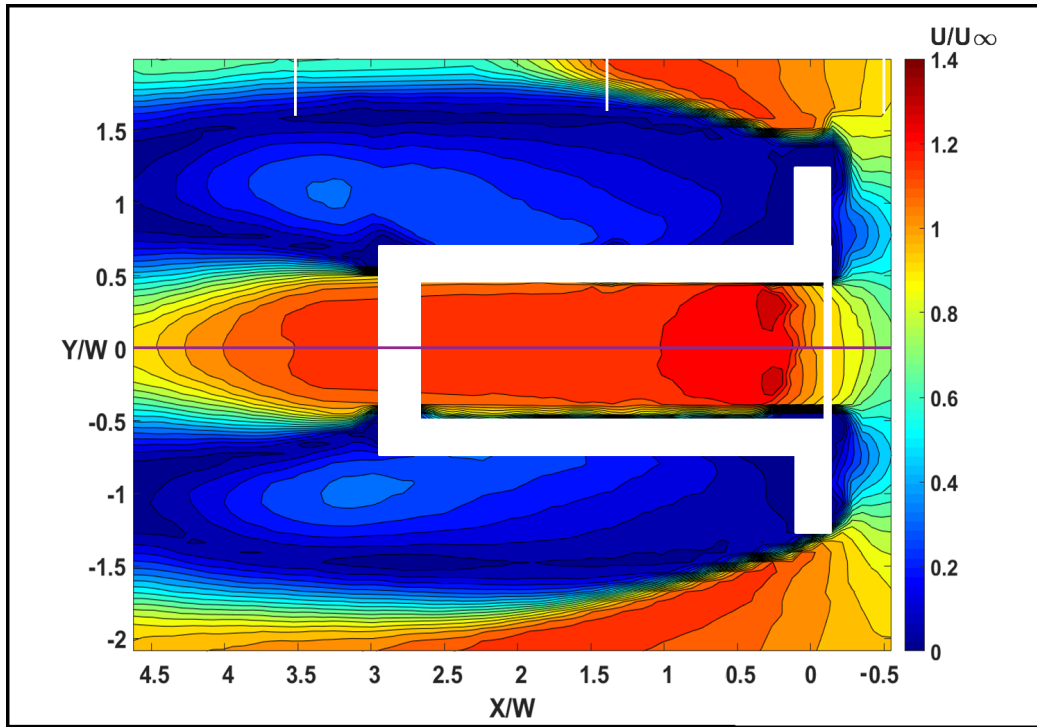


(a)

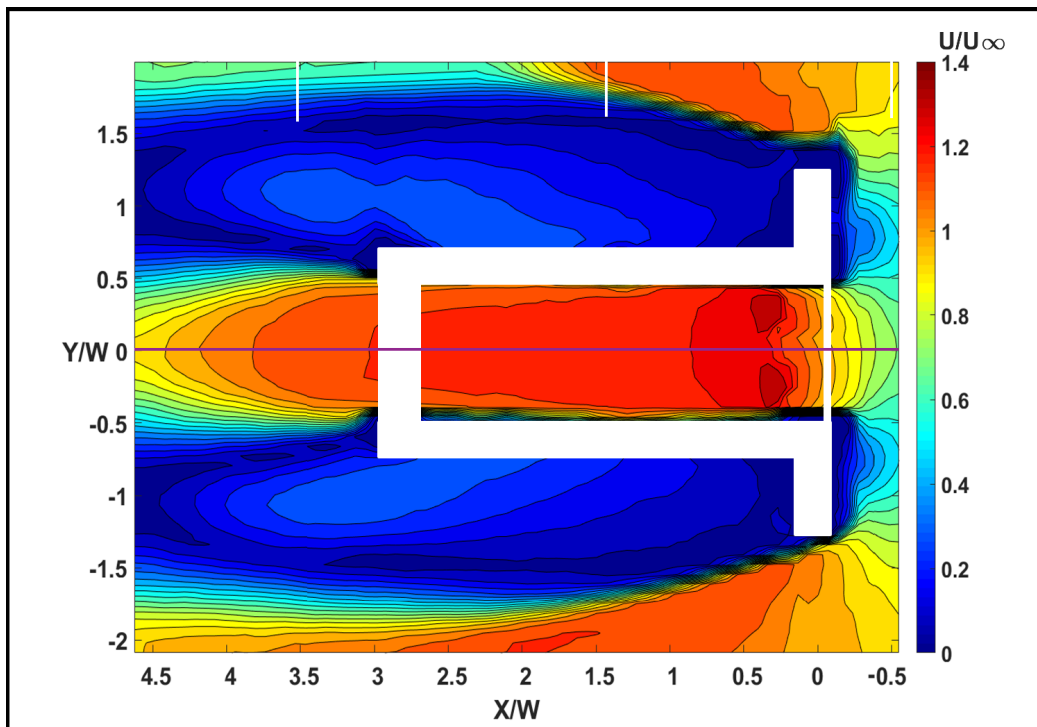


(b)

Figure 2.15: Velocity magnitude contours for the "Flanged" duct geometry in the outlet flange configuration for: (a): Outlet Flange 15Hz and (b): Outlet Flange 30Hz.

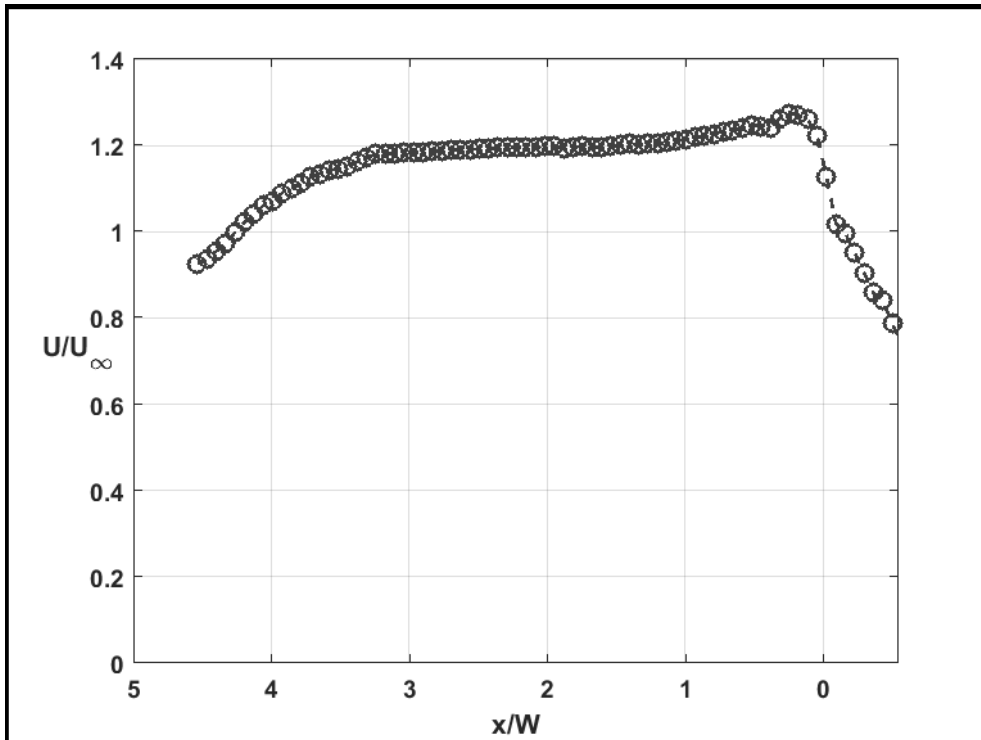


(a)

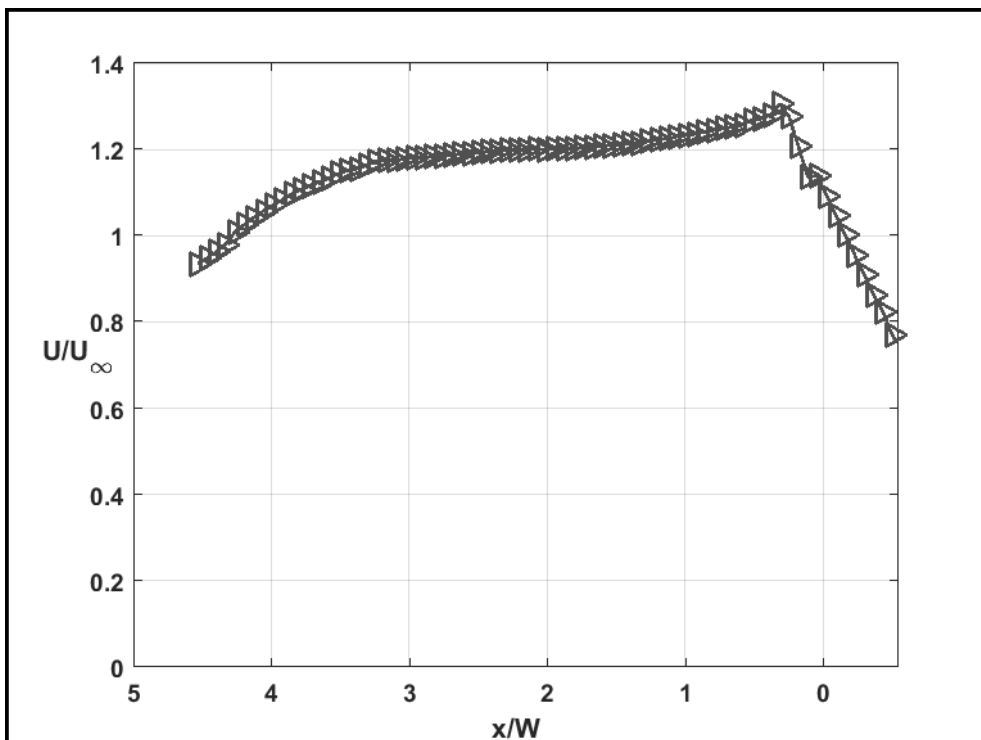


(b)

Figure 2.16: Velocity magnitude contours for the "Flanged" duct geometry in the inlet flange configuration for: (a): Inlet Flange 15Hz and (b): Inlet Flange 30Hz.



(a)



(b)

Figure 2.17: Streamwise velocity magnitude sections for the "Flanged" duct geometry in the inlet flange configuration for: (a): Inlet Flange 15Hz and (b): Inlet Flange 30Hz.

Case	U_∞ (m/s)	In-duct Mean U/U_∞	Percentage Augmented
Plain Duct 15Hz	13.17	1.0495	4.95%
Plain Duct 30Hz	29.44	1.0366	3.66%
Inclined Duct 10deg	13.17	1.1052	10.52%
Inclined Duct 20deg	13.17	1.1714	17.14%
Inclined Duct 30deg	13.17	1.1992	19.92%
Diffuser 15Hz	13.17	1.1182	11.82%
Diffuser 30Hz	29.44	1.1160	11.60%
Nozzle 15Hz	13.17	1.1458	14.58%
Nozzle 30Hz	29.44	1.1386	13.86%
Outlet Flange 15Hz	13.17	1.1333	13.33%
Outlet Flange 30Hz	29.44	1.2083	20.83%
Inlet Flange 15Hz	13.17	1.1960	19.60%
Inlet Flange 30Hz	29.44	1.2077	20.77%

Table 2.2: Augmentation table for all 13 cases discussed in the result section. U_∞ taken from plain cases to avoid larger stagnation effects present in other cases.

In addition, comparing the flange augmentations with [4]’s results and [14]’s designs suggests that although the favored rear-flanged diffuser design does provide a significant augmentation of about 4-5 times the free-stream velocity [4] while maintaining smooth flow into the shroud, a front-mounted flange with a wide duct inlet area, such as a frontal-mounted nozzle enclosure, might provide even more augmentation, especially when the reduced l/W might promote the cross-talk flow and further increase this effect. However, this suggestion requires more speculation in terms of analyzing smaller l/W ratios typical of such turbines, as well as testing several flange widths in terms of duct lengths, as well as the analysis of the rotor placement on such a configuration, all of which might be incorporated in future works. However, the current study does indeed establish improved understanding of the flow dynamics and presents several criteria in selecting the optimal shroud geometry.

2.5 Summary and Conclusions

Wind tunnel velocity field measurements have been acquired for a number of geometric models of the same internal duct geometry with different outer enclosures in a free-stream environment. The study in its basic nature bears relation not only to speed augmentation in ducted wind turbines, but can be also applicable to flow around buildings, jet engine flow dynamics, as well as bluff body aerodynamics. The study aimed to elucidate the effect of the outer duct geometry on the level of flow augmentation inside it. Thus, the internal duct geometry was fixed in all models, and its length-to-width ratio maintained at 3, typically longer than the ratios used in shroud-augmented wind turbines, to reduce the effect of cross-talk between the duct inlet and outlet through the outer flow path. From an inviscid, potential flow viewpoint, the diffuser-type models were expected to create an increased pressure gradient outside the duct that produces flow augmentation internal to the duct, while the nozzle models would create an adverse pressure gradient externally, and produce less flow augmentation. The experimental results, however, demonstrated that the nozzle produced somewhat higher flow augmentation inside the duct than the diffuser model. This indicated that viscous flow effects associated with the creation of a larger shear layer behind the front face of the nozzle, which were not present in the diffuser model, were the cause for the higher flow augmentation. Of particular interest was the significant Reynolds number dependence of the flow augmentation in the outlet flange model. Thus, it can be concluded that Reynolds number effects were of critical importance in this study. Although it might be unclear how the flow augmentation behavior might be at Reynolds number outside the range tested, but in the theoretical limit that Re approaches infinity, the inviscid flow model predictions presented in the literature would be expected to become directly applicable.

The nozzle, diffuser, inlet flange, and outlet flange models in this study had the same blockage ratio of around 1.8%, with the level of flow augmentation varying between 11% and 21%. While these values might seem low as compared to the 70% and 80% presented in the literature, as wind power scales cubically with speed, a 21% increase in wind speed would still produce more than a 75% increase in the available wind power.

The results obtained from the inlet flange case allowed comparison with the results presented in [4], as well as the effects discussed in [14]. Although the rear-mounted flange was found to provide a significant augmentation, a front-mounted flange with a wide duct inlet, namely a front-flanged nozzle, was suggested to possibly provide even more augmentation in the light of the obtained results. The possibility of studying this configuration is presented, along with the addition of future work on multiple flange heights as in [14], as well as the reduction of the length-to-width ratio which would further increase the effect, similar to the

studies in [4] and [49]. Lastly, when there is a turbine or other obstacle in the vicinity of the duct, it is expected to alter the flow dynamics of the empty duct. However, with all else being equal, the current study provides insight into the flow behavior of a duct in free-stream flow. Moreover, the data presented herein may be of help for calibrating and validating numerical models of wind augmentation.

Chapter 3

Flow Visualization in Aortic Dissections

3.1 Introduction

Aortic dissection (AD) is a life threatening cardiovascular disease. A dissection can originate from chest trauma or even a combination of environmental and genetic causes, and is identified by the development of a tear in the innermost layer of the aortic vessel, referred to as the entry tear, permitting the blood to flow between the intimal and medial layers of the arterial wall. Due to the elevated blood pressure and induced wall stress, the tear increases in size, and blood in the aorta separates into two channels, the initial true lumen, and a new false lumen, forming a parallel flow conduit [5],[6],[7]. The false lumen flow can burrow its interstitial path and tear another opening in the intima back into the true lumen flow, typically downstream, denoted as a reentry tear. Two main types of aortic dissections exist, classified according to the location of the tears, with the ones developed in the ascending aorta, classified as Type A dissections, being the more life-threatening. Type A dissections are the more dangerous as the tear can extend to the descending aorta and are usually associated with higher mortality rates. Type B dissections, on the other hand, are limited to the descending aorta and are thus of a reduced level of urgency as compared to type A. It is also possible that thrombus may develop inside the false lumen in both types, leading to blockage of the entry tear and/or reentry tear. The most employed aortic dissection type denotions referred to in the literature are presented in fig. 3.1, as presented by [57]. The designations in this study refer to the Stanford type naming.


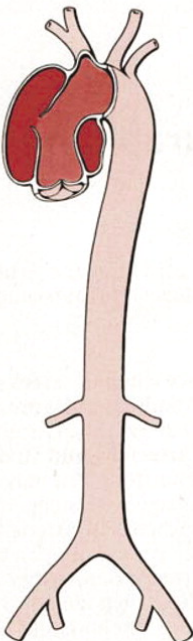
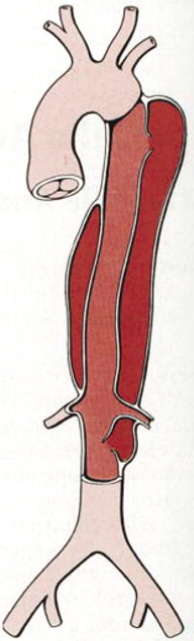
De Bakey Type I	Type II	Type III
		
Stanford	Type A	Type B
<p>De Bakey</p> <p>Type I Originates in the ascending aorta, propagates at least to the aortic arch and often beyond it distally</p> <p>Type II Originates in and is confined to the ascending aorta</p> <p>Type III Originates in the descending aorta and extends distally down the aorta or, rarely, retrograde into the aortic arch and ascending aorta</p> <p>Stanford</p> <p>Type A All dissections involving the ascending aorta, regardless of the site of origin</p> <p>Type B All dissections not involving the ascending aorta</p>		

Figure 3.1: Most common aortic dissection type classification as presented in [57]

Aortic dissection is considered challenging in terms of diagnosis and treatment, thus making it the most complex form of acute aortic syndrome. A dissection may go asymptomatic during its early stages, or even show misleading symptoms that may be mistaken for other conditions within a wide range of cardiothoracic diseases, such as musculoskeletal disorders [58]. An estimated 38% of dissections [58] are not diagnosed from the first testing procedure, and if left untreated at the right time, 36% to 72% of patients die within 48 hours of diagnosis, and 62% to 91% die within one week, due to inflation developing within the aortic vessel, denoted as an aneurysm [58]. Having recorded cases dating back as early as the late 18th century, and having an epidemiology of approximately 30 cases per million per year, it remains at the forefront of medical concern and research [5].

The development of reliable diagnostic-imaging techniques has become paramount to an increased accuracy in detection of possible aortic dissections in order to provide reliable means to their treatment. The three most-employed types of imaging are Trans-Thoracic Echocardiography (TTE), Trans-Esophageal Echocardiography (TEE), Cardiac Computed Tomography (CT), and Magnetic-Resonance Imaging (MRI). Choice of the imaging method used is taken on a case-by-case basis, although other factors such as operation cost and dissection severity are also major contributors. Thorough studies and comparisons of these techniques are available, most notably those performed in [59].

In order to increase diagnostic accuracy through imaging, a reliable aortic model is required. Several studies have been conducted in order to generate accurate aortic models, accounting for different sets of studied variables. Among these studies, the one performed in [60] analyzed the pressure variations inside the aortic true and false lumens in an ex-vivo model for different anatomical configurations of tear size, number, and locations for a Stanford type B dissection. Although Type B dissections were associated with higher survival rates as compared to those of type A, the medical nature of treatment of type B as opposed to the surgical type for A required a more accurate modeling of the flow dynamics, especially the pressure distribution (in relation to the wall shear stress) that directly affected intima tearing and aneurysm growth rate. A pulsatile pump was used in order to mimic heart systole and diastole cycles, as well as an arch and a polymeric silicone tubing with a dissection representing the aortic arch and descending portion. In addition, resistance clamps and a capacitance chamber was used to accurately represent peripheral flow resistance in actual in-vivo blood flow. The perfusion liquid used was a Doppler test liquid at body temperature to mimic blood and obtain more valid results for the pressure distributions. The setup allowed the analysis of the effect of size and location of tears on flow dynamics, and thus compare systolic and diastolic pressures in both true and false lumens.

A more theoretical approach was performed in [61] through a set of CFD simulations in order to predict the hemodynamic forces on the lower aorta pre- and post-treatment of a type B acute aortic dissection using a stent graft. This was done in order to predict the wall shear stresses responsible for aortic ulceration and tear formation in an existing patient on whom CFD model validation was performed. Dynamic MRI imagery was also conducted in order to provide accurate model dimensions for CFD, as well as relevant validation data.

In order to account for the transient nature of blood flow, the hemodynamics of an abdominal aortic aneurysm, by virtue of both steady and pulsatile flow, with a variation of Reynolds number, were explored using PIV in [62]. Significant differences between steady and pulsatile conditions were obtained, especially in the vortex-center dynamics formed in the aneurysm, and the wall shear stress boundary conditions. It was deduced that even though steady flow provided a relatively simple and somewhat accurate insight into the flow dynamics inside aneurysms, it was not sufficient to provide a comprehensive model for the hemodynamics of in-vivo flows.

3.2 Aim of Research

In this study, Computed Tomography (CT) is employed as the reference imaging process as it is the most cost-effective and readily-available diagnostic technique. The first course of diagnostic action is an X-Ray CT scan, used to check for anatomical abnormalities. When dissection or any other condition such as the presence of an aneurysm or a coronary artery blockage is suspected, contrast-injected CT is then employed [8],[9],[10]. In contrast-CT, a reactive contrast-media solution is injected into the blood stream to illuminate the blood vessels being scanned using X-Ray and aid in visualization. The rotating machine continually acquires data during injection, and quantity and rate of injection are normally elevated to improve image quality. However, this may present an issue as the fluid solution may have adverse effects on the patients health [63]. In addition, despite CT scanning being an established technique, false diagnosis, such as a false positive and a false negative, from contrast-CT imaging can be quite common [11],[12]. Therefore, and in accordance with the bio-inspired research process and based on the request of the radiology department in the AUBMC, a better understanding of the hemodynamics inside the aortic arch for different dissection configurations is required to assist in improving diagnostic accuracy.

In contrast-CT administration, a delicate balancing act is performed by the radiologist in order to optimize the injection parameters. Synchronization of the injection timing with the scanner head has to be coupled with several factors, including the patients weight, heart rate, blood flowrate, and pulmonary rhythms [64]. The interconnected biological systems make the process tedious, and thus it is of importance that the hemodynamics, as well as the transport and mixing mechanics of the contrast media in the blood stream within the complex aortic dissection geometry be understood [65],[66],[67],[68],[69]. The quality of the contrast-CT images is dependent on the combination of the CT scanning speed and the speed of the bloodstream in the aorta, where flow details such as mixing dynamics and contrast flow-front dynamics may or may not appear according to the size of the temporal resolution utilized.

In order to accurately predict the existence and location of aortic dissections, especially acute types, better understanding of the fluid dynamics inside the aorta is required. One of the main causes of tear formation is the excessive wall shear stress on the intima, focused mainly downstream from the aortic valve. As the intima is a thin, soft layer, it is most susceptible to stress and thus tears quickly, leading to aortic intramural hematoma. The main imaging techniques proposed for this purpose are PIV and LIF, which will allow the generation of an accurate aortic flow and comparability with CT results.

3.3 Methods

Simplified plexi-glass models representative of different aortic dissection scenarios are constructed and connected to a steady-flow loop system. These models are then subjected to flow conditions similar to those in an actual aorta. Two imaging techniques, PIV and LIF, are then utilized to assess the flow and to visualize the transport dynamics of the injected contrast media, as shown in fig. 3.2. PIV is employed and allows to obtain a quantitative field of the behavior of the flow throughout the different lumens, while LIF is used as the main imaging technique due to its comparability with the CT scanner used on actual dissections. LIF allows the visualization of flow development, vortex shedding, as well as residency time calculation through the manipulation of the corresponding luminosity fields. As a proxy for CT imaging with contrast injection, LIF is used with high-speed CCD imaging to record the mixing dynamics of dye in the dissection and is used to compare with an actual CT scan of the model in order to locate similarities and allow radiologists to more accurately diagnose aortic dissections.

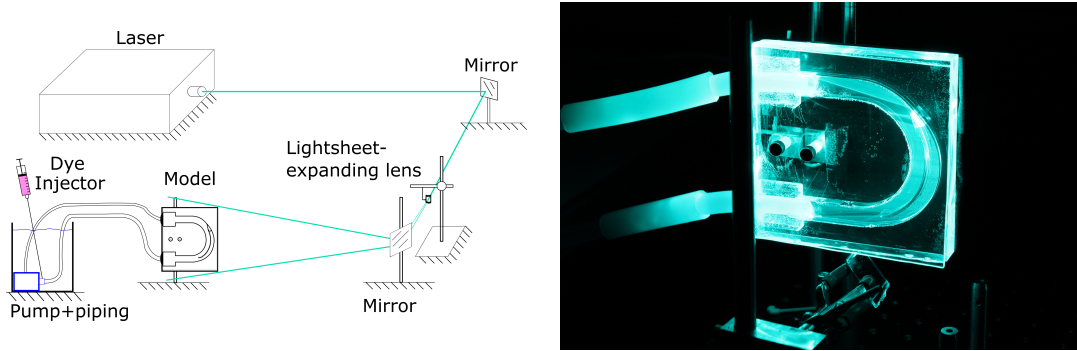
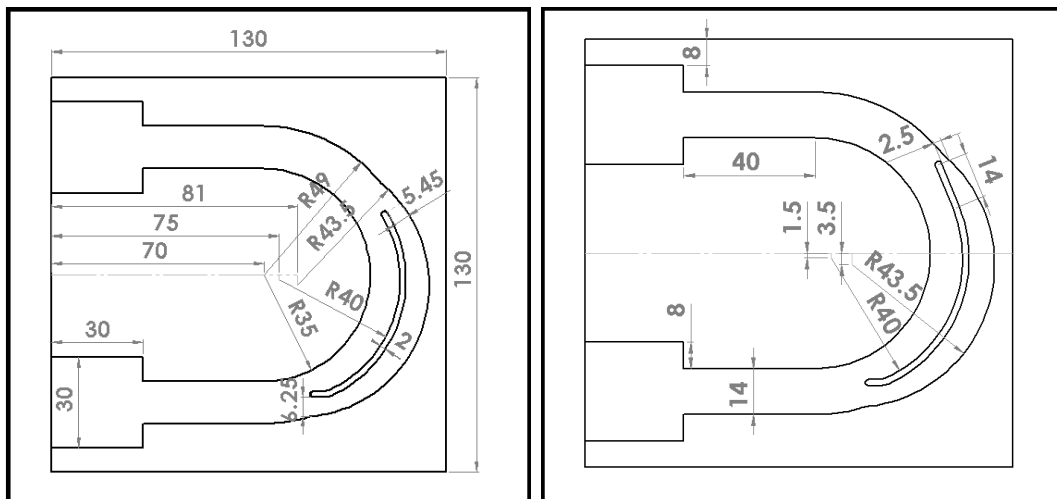


Figure 3.2: (left) Schematic of the AD flow loop and the laser diagnostic system for PIV and LIF; (right) a picture of an AD model installed in the test setup

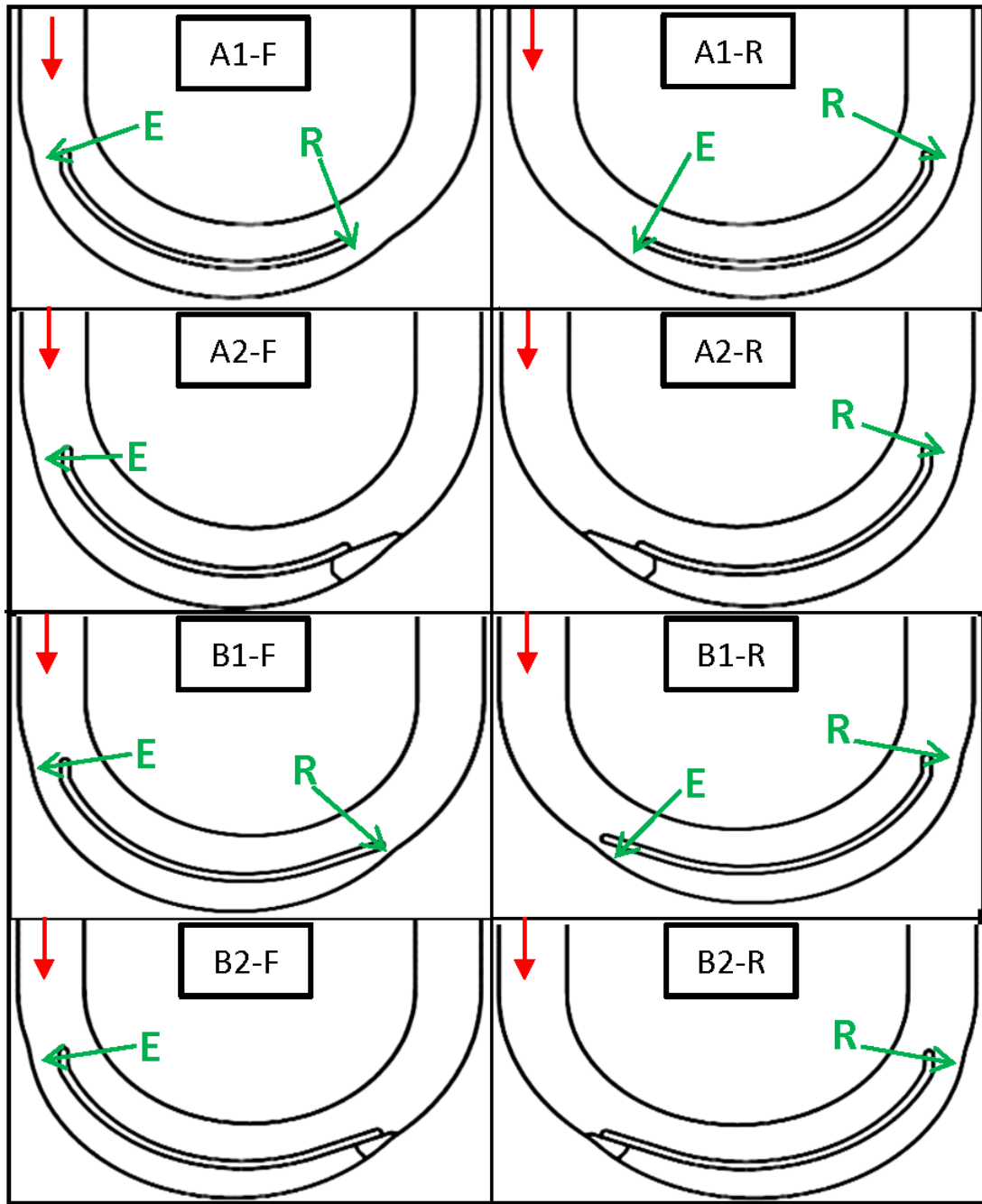
3.3.1 Dissection Models and Flow Loop:

Type A Dissections, which affect the ascending aorta, are studied in this setup. The aortic model constitutes of a planar bend with a 35mm radius of curvature and a square cross-section of 14mm side length at its proximal and distal ends. Two models are machined from optically clear plexi-glass and their surfaces are polished for flow visualization, shown in fig. 3.3a. The case designations are then categorized into Model A and Model B designations, based on the size of the machined re-entry channel, with Model B having the smaller channel. A plexi cover is then glued using clear polyurethane liquid and the inlet and outlet pipe fittings are installed and connected to a submersible centrifugal pump (5 W) in a water reservoir symbolizing body peripheral flow. Although the flaps and intimal walls in an actual aorta can flutter in response to the underlying flow field, the

models presented here have rigid features maintained in order to minimize the handled variables. The models constitute several combinations of an entry tear with or without a reentry tear, with a corresponding suffix assigned to differentiate each case. Cases where the re-entry tear is present are assigned the suffix 1, while those having this channel sealed are assigned the suffix 2. The models may also have either an entry or a re-entry tear flap protruding into the flow. These cases are achieved through the variation of flow direction, allowing the manipulation of the type of entry and thus allowing a larger spectrum of dissection cases to be represented. In accordance, configurations having an entry-flap are shown as -F, while the others are shown as -R. As a result, a total of eight disease scenario geometries are generated from the two physical models, presented in fig. 3.3b. In the left column, cases A1-F, A1-R, B1-F, and B1-R are of the entry-reentry AD type, while in the right column, cases A2-F and B2-F are of the entry only type, and cases A2-R and B2-R are of the re-entry only type. The bulk flow rate in all cases is measured to be 3 L/min and varies by less than 5% across.



(a)



(b)

Figure 3.3: (a) Dimensioned drawings of the two machined AD models. The channel is 14 mm deep. (b) Eight test cases are investigated with the red arrow symbolizing flow direction. (E) is designated for entry-tear cases, and (R) for reentry tear cases. There are four cases with entry tear flap (*left*) and four with reentry tear flap (*right*). Each flow geometry is labeled.

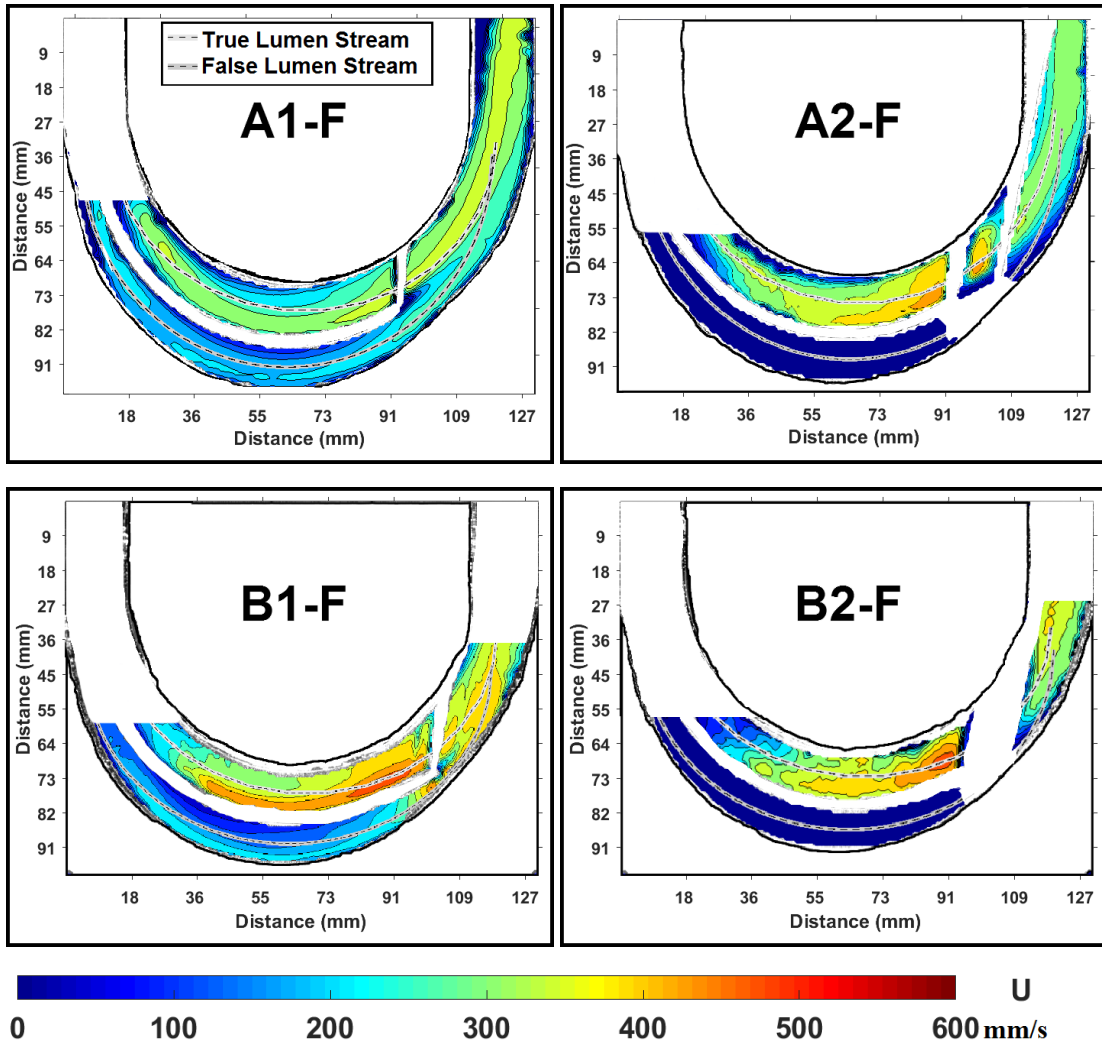
3.3.2 PIV and LIF Measurements:

The laser beam from a 3 W Ar-ion laser (Laser Physics, UK) is steered and expanded through a set of lenses and mirrors into a 1mm-thick lightsheet that illuminates a plane at mid-height of the aortic model, as shown in fig. 3.2. A Phantom V9 CCD camera (Vision Research, USA) images the flow illuminated by the lightsheet at 200 fps for LIF and 1000 fps for PIV. A Schott-glass long pass orange filter covers the camera to permit only the light wavelength from the Rhodamine fluorescence during LIF acquisition. Rhodamine dye solution (5 mL volume) is injected at the suction side of the submerged pump for a duration of 3 sec, i.e. with a flow rate of 100 mL/min. The camera sequence commences before the dye reaches the aorta and continues well after the injection process completes. This is necessary to correct for spatial lightsheet intensity variations. For the non-simultaneous PIV, the flow is seeded with $5\mu\text{m}$ TiO_2 particulate powder. Around 1000 consecutive particle images covering 1 second of flow data are processed with the Matlab-based FFT cross correlation code PIVLAB [70] to produce 500 velocity vector fields. The spatial vector resolution is approximately 1.5 mm, which is found sufficient to resolve the main flow velocities in the false and true lumens. The instantaneous velocity vector fields are averaged to produce a mean vector field.

3.4 Results

After the PIV processing to all the desired cases, post-processing algorithms are applied in order to further reduce erroneous vector fields and yields smoother velocity transitions. Among these processes, scatter-plot elimination is utilized in order to remove out-of-range vectors and reduce the total standard deviation. In addition, spatial filtering is then applied to vectors failing to satisfy the median $\pm n \cdot Stdev$ condition, with n set to 2. Finally, the time-averaged velocity contours obtained from PIV processing are then presented for the eight dissection cases, as shown in fig. 3.4. The cases are divided into two types according to the intended model scheme: Configurations with an entry-tear flap, presented in fig. 3.4a, and ones with a re-entry-tear flap, as in fig. 3.4b. For the cases in fig. 3.4a, the models may or may not include a re-entry tear, which allows the blood flow to enter from the main vessel to the false lumen and exit back into the true lumen downstream. Models A1-F and B1-F are of the entry-reentry AD type, with the reentry tear size for case B1-F being narrower. A salient feature noted in these models is the dissimilar velocities in the false lumen as compared to the true lumen, with the difference being larger for the smaller reentry of model B. The velocity magnitudes along the two dashed-black lines plotted in fig. 3.5a further confirm this observation. However, due to light diffraction and blockage by the sharp interfaces near the flap and at the end of false lumen walls, some portions of the field do not resolve to consistent velocity vectors, and are hence masked. In accordance, upon reentry to the true lumen, the two dissimilar blood streams would theoretically form a shear layer. This is indeed observed in the instantaneous LIF images shown in fig. 3.6a. The unsteadiness associated with the shear layer, in addition to the three-dimensional curvature flow exhibited in the aorta can thus induce unsteady loading on the tear and cause it to widen, forcing more flow into the false lumen and possibly creating an oscillatory-flapping re-entry tear.

For the other two entry-tear cases in fig. 3.4a, models A2-F and B2-F exhibit an entry-only flow, where the re-entry tear is blocked off, symbolizing the presence of a thrombus. In these cases, the flow is completely stagnant in the false lumen, except for hints of weak recirculating flow near the entry flap. LIF imaging indicates that entry flow from the true lumen penetrates to a certain depth into the false lumen, as shown in fig. 3.6b. This flow deceleration to stagnation is associated with an increase in the false lumen average pressure as compared with that of the true lumen, as has been studied in [60] and [71]. This local pressure increase can contribute to further weakening of the intimal aortic wall and enlargement of the dissection canal.



(a)

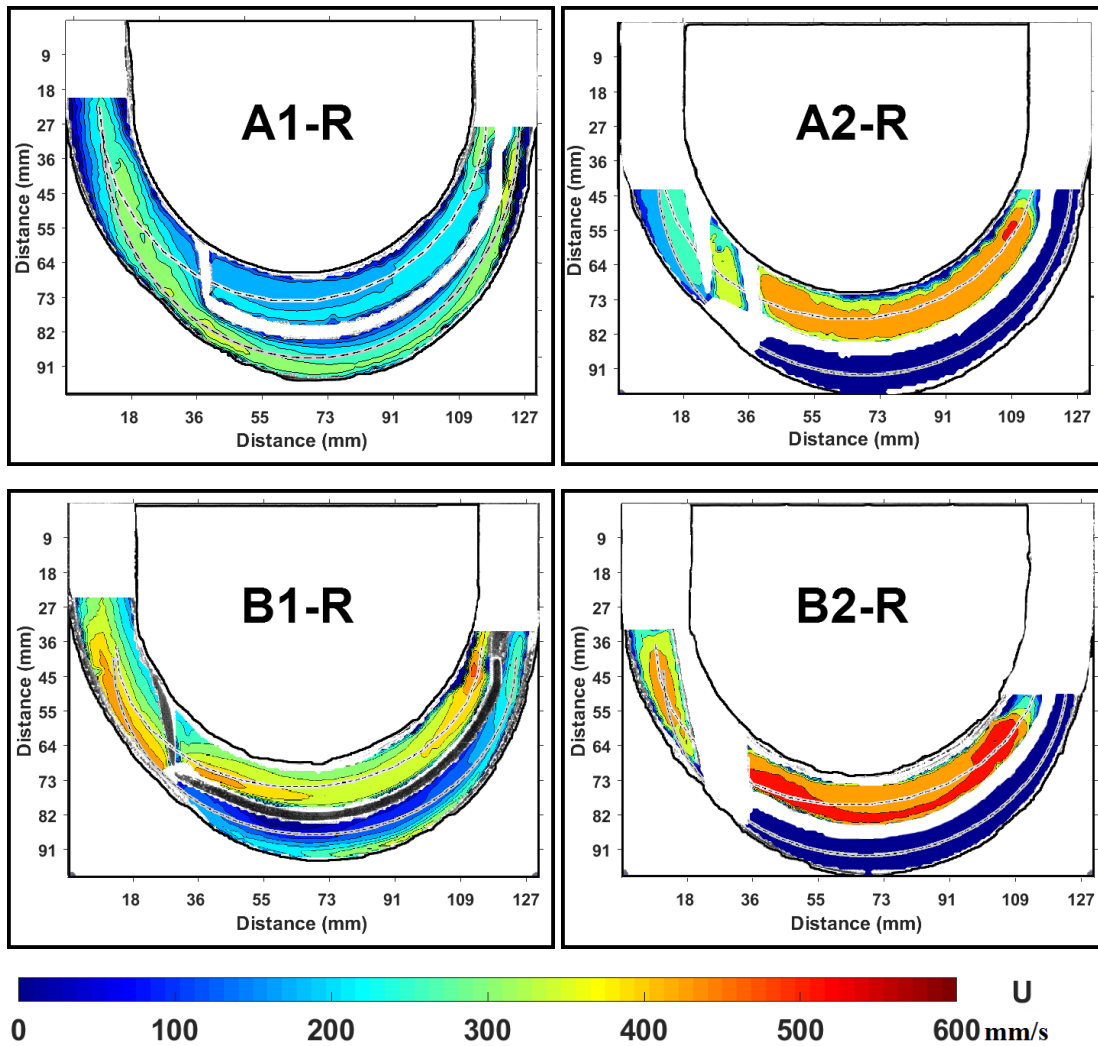
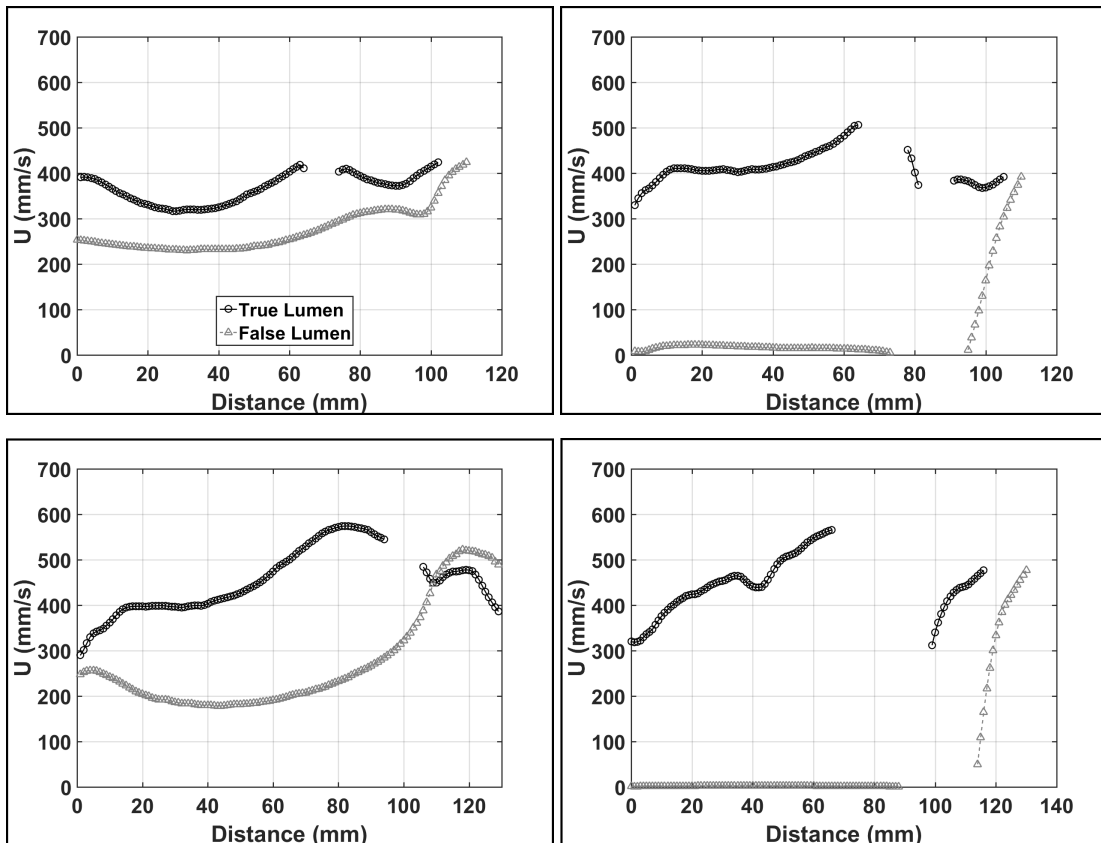


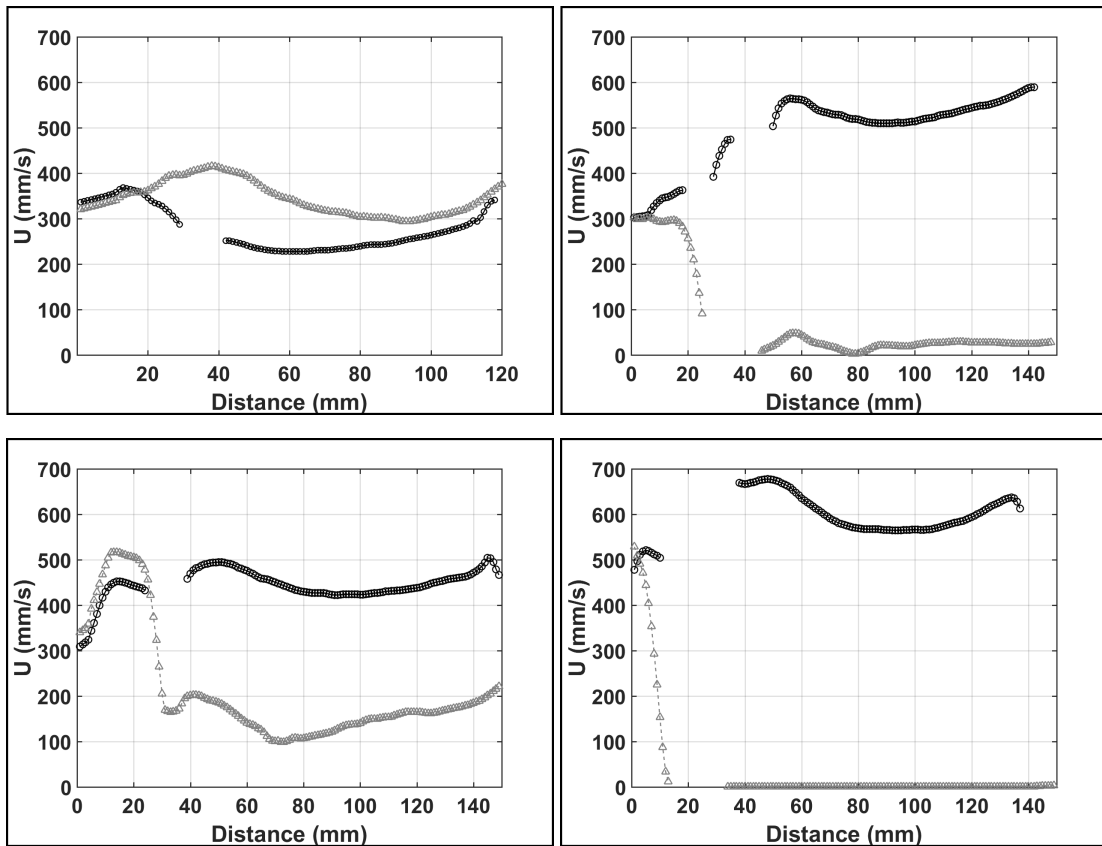
Figure 3.4: Velocity magnitude contours for (a) the four models with entry flap, and (b) the four models with the re-entry flap. Color scale is in mm/sec.

The four models presented in fig. 3.4b have re-entry tear flaps protruding into the flow, while the entry tears are smaller in size and are shifted downstream in comparison with the cases in fig. 3.4a. Yet, the salient flow features in fig. 3.4 are generally similar, except for structural variations associated with changes in local geometry. This assessment is generally substantiated by the velocity magnitude plots in fig. 3.5 and the instantaneous LIF flow front images in fig. 3.7. The flow front discussed here refers to the time when the dye first reaches the aorta from the peripheral injection point, with the contrast intensity being elevated and clearly visible. Of particular interest in the LIF instantaneous images of fig. 3.7 is the visibility of the false lumen region. When the AD is of the entry-reentry type, the fluorescent Rhodamine dye, surrogate for contrast CT media, perfuses

sufficiently into the false lumen making it visible, albeit at a slower rate than in the true lumen by virtue of the dissimilar flow velocities. However, if the false lumen is of the entry-only or reentry-only types, the probability of the dye perfusing into the false lumen and making a noticeable mark in the images is quite low. In the context of contrast-CT patient diagnostics, this may make the difference between a correct diagnosis and a false diagnosis.

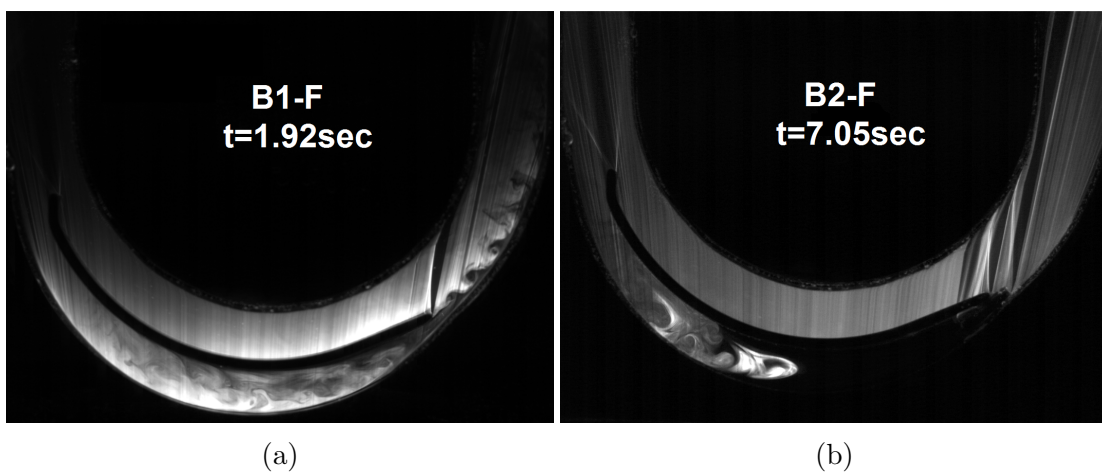


(a)



(b)

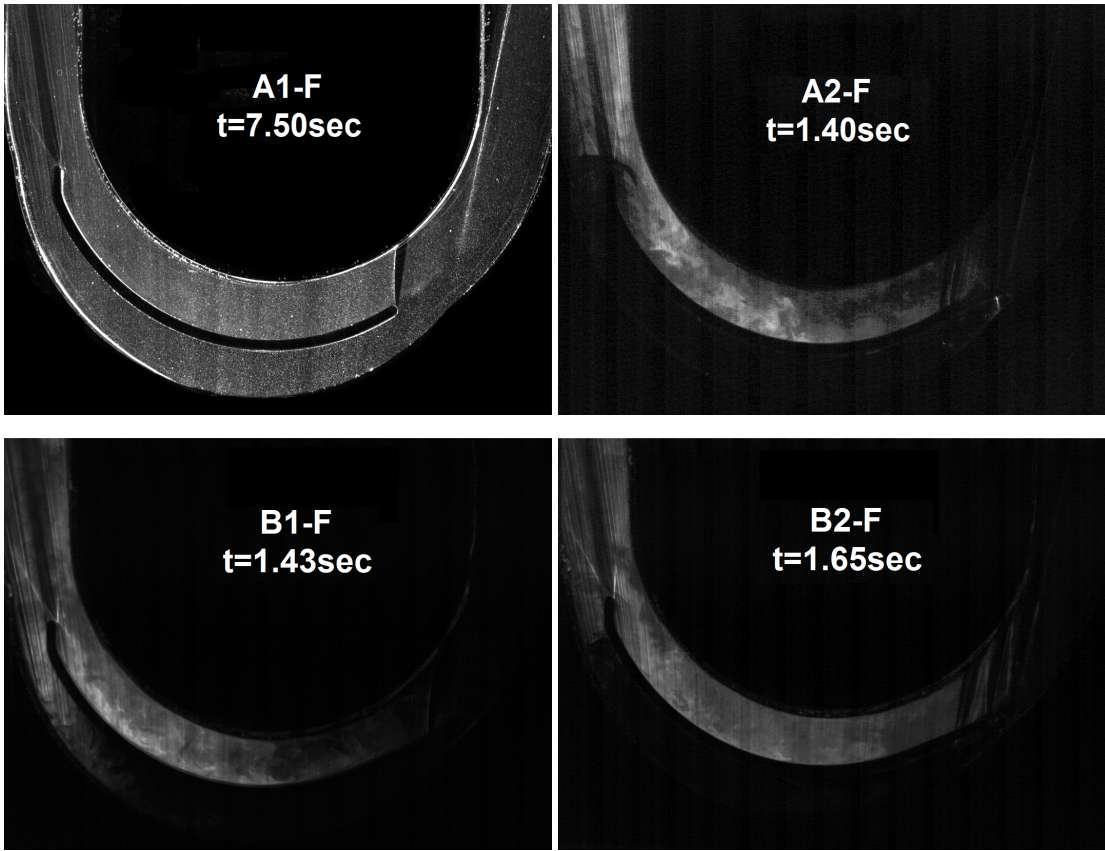
Figure 3.5: Flow velocity magnitude in the true (black) and false (gray) lumens for (a) the four models with entry flap, and (b) the four models with the re-entry flap. Plot order follows that in fig. 3.4



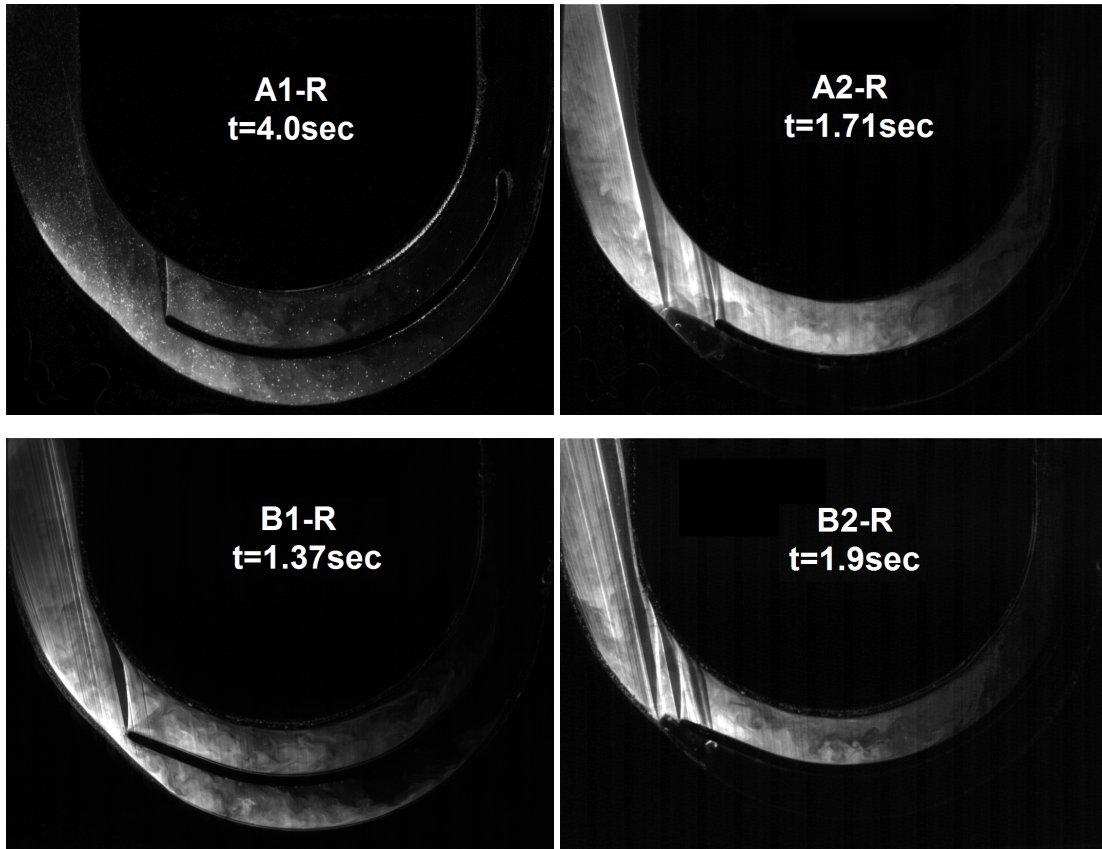
(a)

(b)

Figure 3.6: (a) Instantaneous LIF images showing the shear layer in an entry-reentry AD; (b) the penetration of the entry flow into the stagnant false lumen blood.



(a)



(b)

Figure 3.7: Instantaneous LIF images of the dye bolus flow front for (a) the four AD cases with entry flap, and (b) the four cases with the re-entry flap. The time stamp corresponds to the plots in fig. 3.9.

In order to be able to setup an accurate comparison of the generated data with results from contrast-CT scans, the time traces of the LIF signal are spatially-averaged over local regions of the AD, with their respective temporal intensities plotted over the course of the entire injection process. The signals are also post-corrected for spatial variations in lightsheet intensity using a linear-correction curve, which requires the determination of a slope and an intercept. The linear correction assumes negligible auto-bleaching and self-absorption of the LIF emissions. Fig. 3.8a shows the LIF intensity plots prior to correction. The pre-injection part of the curve is used to determine the non-zero background signal, taken as the intercept of the correction line, while the farthest post-injection part of the curve with a uniform spatial-dye distribution is used to determine the slope of the correction line. The LIF data after correction are applied and shown in fig. 3.8b, which demonstrates that before injection, the LIF signal in all regions begins at zero, and once the dye is fully mixed towards the end, all signals converge to the same value.

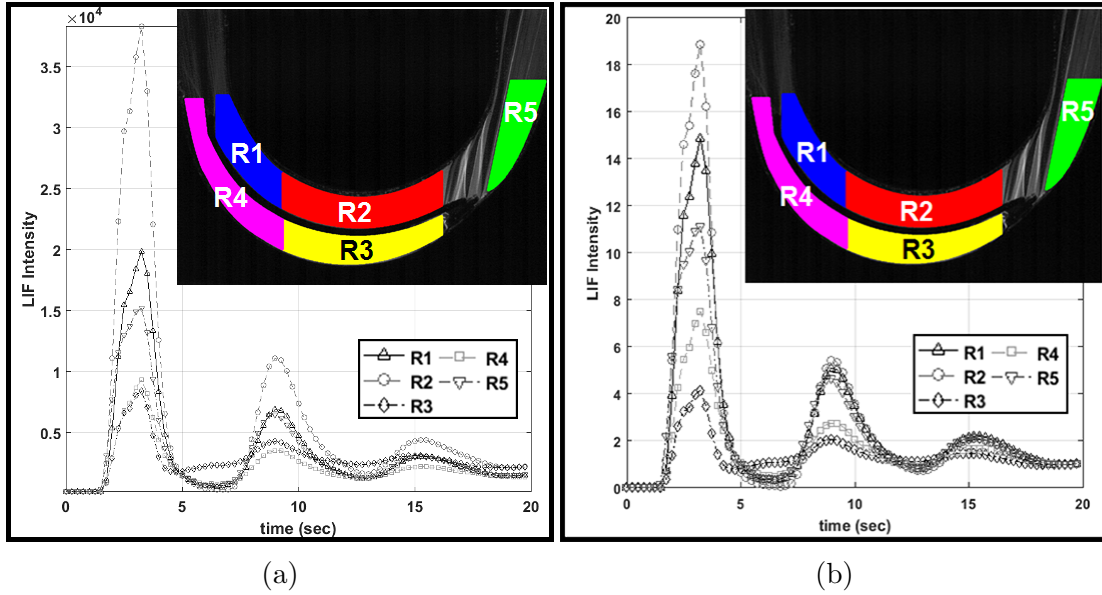
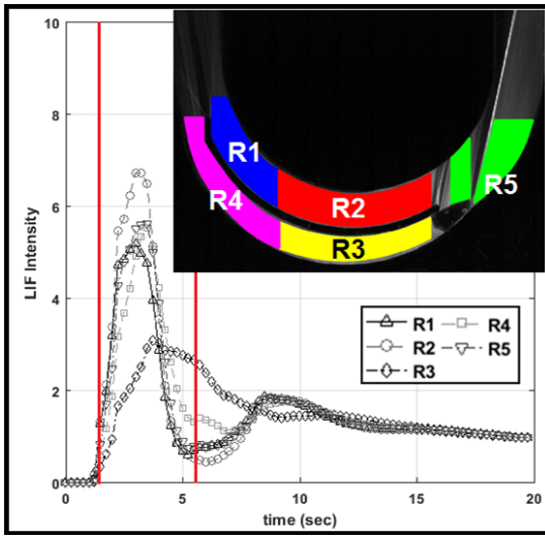
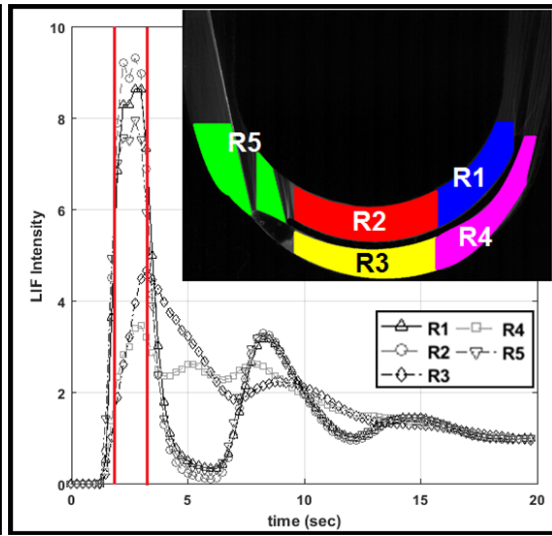


Figure 3.8: Spatially-averaged LIF time trace signal for AD case B2-F (a): uncorrected; and (b): linearly-corrected for light sheet intensity variations.

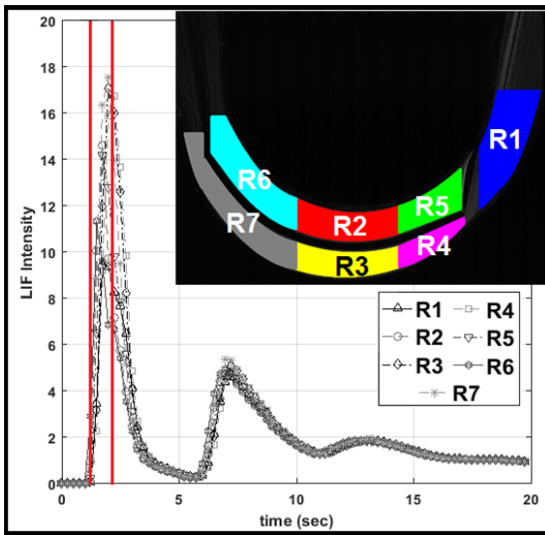
In fig. 3.9, the corrected dye-concentration time traces are shown for six cases of AD. Data for the remaining two cases are insufficient for correction due to the limited recording length, and thus they are not presented. For each case, the AD regions used for spatial averaging are delineated on the same corresponding figure. In all the AD cases, with a focus on the true lumen, the LIF signal builds up as the dye bolus reaches the aorta, and once injection stops, the signal drops significantly, until the dye makes a full circle through the reservoir and pump, and circulates back to the AD, albeit at a much lower concentration due to mixing. In the entry-reentry cases, the signal from the false lumen is generally in-phase with the true lumen signal, but with an overall lower intensity due to the slower false lumen velocity and local dye dilution within it. In the AD cases with an entry-only or reentry-only type, the intensity difference is still present, although now, there is a significant phase difference or delay between the intensity peaks of both lumens. This observation is expected since the dye takes more time to penetrate the false lumen and a significantly larger period to dissipate through the slow mixing processes of the creeping flow inside the lumen.



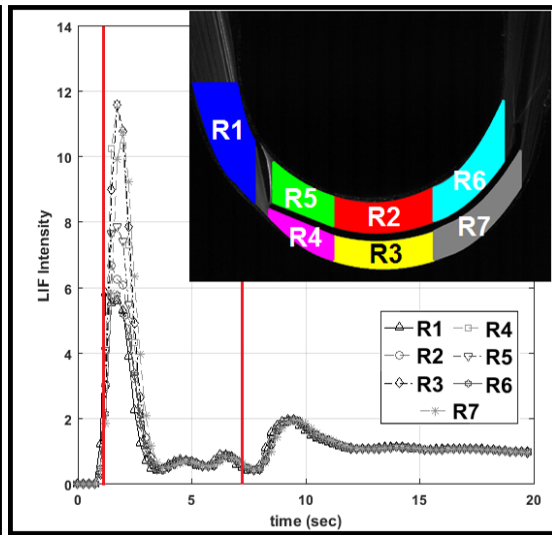
(a)



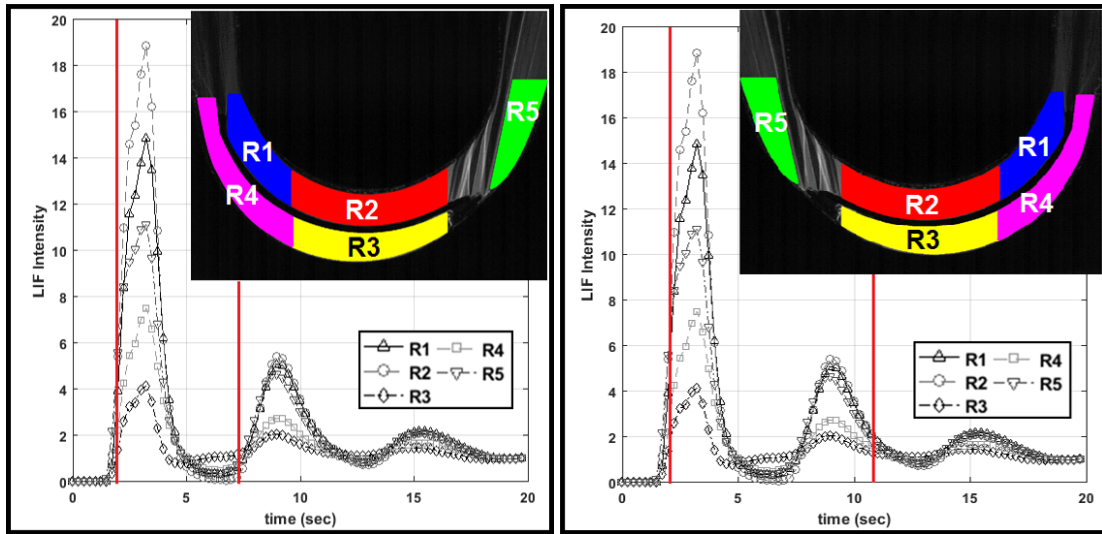
(b)



(c)



(d)



(e)

(f)

Figure 3.9: Spatially-averaged and intensity-corrected LIF time trace signals for six AD cases: (a): A2-F, (b): B1-F, (c): B2-F, (d): A2-R, (e): B1-R, (f): B2-R. Red lines are time stamps corresponding to figs. 3.6, 3.7

3.5 Summary and Conclusions

Eight in-vitro study cases of Type-A aortic dissections are evaluated using PIV and LIF. These cases cover scenarios with two widths of tears, several dissection configurations such as entry-reentry tears, entry-only, and even reentry-only tears, similar to actual dissection cases, as well as different tear-flap position variants, such as those with a protruding entry tear flap, or a reentry tear flap. In the entry-reentry AD cases, the flow velocities in the true and false lumens are found to be dissimilar giving rise to shear-layer formation upon reentry. This could thus be a flow mechanism that contributes to aortic-wall weakening and AD expansion. In entry-only AD cases, LIF visualization shows the flow penetration into the false lumen before being halted. This flow stoppage is associated with stagnation pressure and is consistent with other reports in the literature on the increased pressure values in the false lumen, another mechanism thought to contribute to AD expansion.

Lastly, there are limitations associated with certain choices made in the design of this work that may not be physiologically accurate. One is the planar curvature of the aorta and its rectangular cross-section. While both are chosen to assist in flow visualization, the rigid model walls do not allow for fluttering, or for tear-flapping, which is often seen in patient diagnosis. Moreover, the flow is chosen to be steady rather than pulsatile in order to reduce varying parameters. In spite of these limitations, these simplified AD geometries do provide an improved understanding of the nature of the flow in a Type-A dissection and its salient features.

Chapter 4

Conclusions

In this dissertation, the flow dynamics of two selected applications are studied through experimental fluid dynamics, with each study composing its corresponding chapter. These applications consist of the analysis of flow augmentation as a function of shrouding geometry in a free-stream, inspired by ducted wind turbines and urban design, as well as the study of a Type A aortic dissection and the generation of a flow model having high comparability with the available CT-scanning machine results. Experimental methods were chosen as they provide the most realistic approach to modeling real-flow problems. Established imaging techniques such as PIV and LIF are utilized in order to measure velocity data with a high fidelity as well as to monitor the salient flow features describing the flows. Indeed, the analysis of the behavior of different shroudings allowed to generate an idea on the possible optimal configuration for augmenting free-stream flows that might be somewhat different to what has been already adopted. In addition, the employment of the LIF technique in the aortic dissection chapter allowed a significant level of comparability with CT scanning that elucidated several key flow features related to different dissection configurations, assisting radiologists in the field and allowing them to increase diagnostic accuracy. Finally, the models created in these studies are not constraint to their respective applications, but may be applied to a wider range of wind energy and bio-inspired projects by virtue of the versatility of the employed flow-imaging techniques.

Bibliography

- [1] R. J. Adrian, “Particle-imaging techniques for experimental fluid mechanics,” *Annual review of fluid mechanics*, vol. 23, no. 1, pp. 261–304, 1991.
- [2] C. Tropea and A. L. Yarin, *Springer handbook of experimental fluid mechanics*, vol. 1. Springer Science & Business Media, 2007.
- [3] M. Raffel, C. E. Willert, S. Wereley, and J. Kompenhans, *Particle image velocimetry: a practical guide*. Springer, 2013.
- [4] Y. Ohya, T. Karasudani, A. Sakurai, K.-i. Abe, and M. Inoue, “Development of a shrouded wind turbine with a flanged diffuser,” *Journal of wind engineering and industrial aerodynamics*, vol. 96, no. 5, pp. 524–539, 2008.
- [5] W. C. Roberts, “Aortic dissection: Anatomy, consequences, and causes,” *American Heart Journal*, vol. 101, no. 2, pp. 195 – 214, 1981.
- [6] J. Golledge and K. A. Eagle, “Acute aortic dissection,” *The Lancet*, vol. 372, no. 9632, pp. 55–66, 2008.
- [7] T. Tsai, S. Trimarchi, and C. Nienaber, “Acute aortic dissection: perspectives from the international registry of acute aortic dissection (irad),” *European Journal of Vascular and Endovascular Surgery*, vol. 37, no. 2, pp. 149–159, 2009.
- [8] M. A. McMahon and C. A. Squirrell, “Multidetector ct of aortic dissection: a pictorial review,” *Radiographics*, vol. 30, no. 2, pp. 445–460, 2010.
- [9] A. Abbas, I. Brown, C. Peebles, S. Harden, and J. Shambrook, “The role of multidetector-row ct in the diagnosis, classification and management of acute aortic syndrome,” *The British journal of radiology*, vol. 87, no. 1042, p. 20140354, 2014.
- [10] P. Nagpal, A. Khandelwal, S. S. Saboo, G. Bathla, M. L. Steigner, and F. J. Rybicki, “Modern imaging techniques: applications in the management of acute aortic pathologies,” *Postgraduate medical journal*, pp. postgradmedj–2014, 2015.

- [11] I. Asouhidou and T. Asteri, “Acute aortic dissection: be aware of misdiagnosis,” *BMC research notes*, vol. 2, no. 1, p. 25, 2009.
- [12] M. Kurabayashi, N. Miwa, D. Ueshima, K. Sugiyama, K. Yoshimura, T. Shimura, H. Aoyagi, K. Azegami, K. Okishige, and M. Isobe, “Factors leading to failure to diagnose acute aortic dissection in the emergency room,” *Journal of cardiology*, vol. 58, no. 3, pp. 287–293, 2011.
- [13] W. Yang, P. J. Tavner, C. J. Crabtree, Y. Feng, and Y. Qiu, “Wind turbine condition monitoring: technical and commercial challenges,” *Wind Energy*, vol. 17, no. 5, pp. 673–693, 2014.
- [14] M. Kardous, R. Chaker, F. Aloui, and S. B. Nasrallah, “On the dependence of an empty flanged diffuser performance on flange height: Numerical simulations and piv visualizations,” *Renewable energy*, vol. 56, pp. 123–128, 2013.
- [15] I. Paraschivoiu, *Wind turbine design: with emphasis on Darrieus concept*. Presses inter Polytechnique, 2002.
- [16] W. Tong, *Wind power generation and wind turbine design*. WIT press, 2010.
- [17] R. Griffiths and M. Woollard, “Performance of the optimal wind turbine,” *Applied Energy*, vol. 4, no. 4, pp. 261–272, 1978.
- [18] S. Sanaye and A. Hassanzadeh, “Multi-objective optimization of airfoil shape for efficiency improvement and noise reduction in small wind turbines,” *Journal of Renewable and Sustainable Energy*, vol. 6, no. 5, p. 053105, 2014.
- [19] A. Wright and D. Wood, “The starting and low wind speed behaviour of a small horizontal axis wind turbine,” *Journal of Wind Engineering and Industrial Aerodynamics*, vol. 92, no. 14, pp. 1265–1279, 2004.
- [20] K. Ameku, B. M. Nagai, and J. N. Roy, “Design of a 3kw wind turbine generator with thin airfoil blades,” *Experimental thermal and fluid science*, vol. 32, no. 8, pp. 1723–1730, 2008.
- [21] D. Lobitz, P. Veers, and P. Migliore, “Enhanced performance of hawts using adaptive blades,” tech. rep., Sandia National Laboratory, 1996.
- [22] S. Daynes and P. M. Weaver, “A morphing wind turbine blade control surface,” in *ASME 2011 Conference on Smart Materials, Adaptive Structures and Intelligent Systems, Scottsdale, AZ, September*, pp. 18–21, 2011.
- [23] A. Kusiak and Z. Song, “Design of wind farm layout for maximum wind energy capture,” *Renewable Energy*, vol. 35, no. 3, pp. 685–694, 2010.

- [24] Y. Chen, H. Li, K. Jin, and Q. Song, “Wind farm layout optimization using genetic algorithm with different hub height wind turbines,” *Energy Conversion and Management*, vol. 70, pp. 56–65, 2013.
- [25] F. del Jesus, M. Menéndez, R. Guanche, and I. J. Losada, “A wind chart to characterize potential offshore wind energy sites,” *Computers & Geosciences*, vol. 71, pp. 62–72, 2014.
- [26] W. T. Pennell, W. R. Barchet, D. L. Elliott, L. L. Wendell, and T. R. Hiester, “Meteorological aspects of wind energy: Assessing the resource and selecting the sites,” *Journal of Wind Engineering and Industrial Aerodynamics*, vol. 5, no. 3-4, pp. 223–246, 1980.
- [27] R. Van Haaren and V. Fthenakis, “Gis-based wind farm site selection using spatial multi-criteria analysis (smca): Evaluating the case for new york state,” *Renewable and Sustainable Energy Reviews*, vol. 15, no. 7, pp. 3332–3340, 2011.
- [28] A. Bennui, P. Rattanamanee, U. Puetpaiboon, P. Phukpattaranont, and K. Chetpattananondh, “Site selection for large wind turbine using gis,” in *PSU-UNS International Conference on Engineering and Environment*, pp. 561–566, 2007.
- [29] K. H. Wong, W. T. Chong, N. L. Sukiman, S. C. Poh, Y.-C. Shiah, and C.-T. Wang, “Performance enhancements on vertical axis wind turbines using flow augmentation systems: A review,” *Renewable and Sustainable Energy Reviews*, vol. 73, pp. 904–921, 2017.
- [30] M. Blanch, “Wind energy technologies for use in the built environment,” *Wind Engineering*, vol. 26, no. 3, pp. 125–143, 2002.
- [31] B. Ovgor, S.-K. Lee, and S. Lee, “A method of micrositing of wind turbine on building roof-top by using joint distribution of wind speed and direction, and computational fluid dynamics,” *Journal of mechanical science and technology*, vol. 26, no. 12, p. 3981, 2012.
- [32] W. Chong, A. Fazlizan, S. Poh, K. Pan, and H. Ping, “Early development of an innovative building integrated wind, solar and rain water harvester for urban high rise application,” *Energy and Buildings*, vol. 47, pp. 201–207, 2012.
- [33] W. T. Chong, S. Yip, A. Fazlizan, S. C. Poh, W. P. Hew, E. P. Tan, and T. Lim, “Design of an exhaust air energy recovery wind turbine generator for energy conservation in commercial buildings,” *Renewable energy*, vol. 67, pp. 252–256, 2014.

- [34] A. B. Tabrizi, J. Whale, T. Lyons, and T. Urmee, “Performance and safety of rooftop wind turbines: Use of cfd to gain insight into inflow conditions,” *Renewable Energy*, vol. 67, pp. 242–251, 2014.
- [35] S. Zanforlin and S. Letizia, “Improving the performance of wind turbines in urban environment by integrating the action of a diffuser with the aerodynamics of the rooftops,” *Energy Procedia*, vol. 82, pp. 774–781, 2015.
- [36] K. Foreman, B. Gilbert, and R. Oman, “Diffuser augmentation of wind turbines,” *Solar Energy*, vol. 20, no. 4, pp. 305–311, 1978.
- [37] A. Grant, C. Johnstone, and N. Kelly, “Urban wind energy conversion: The potential of ducted turbines,” *Renewable Energy*, vol. 33, no. 6, pp. 1157–1163, 2008.
- [38] R. J. Platt Jr, “Static tests of a shrouded and an unshrouded propeller,” 1948.
- [39] R. Flack, “Laser velocimeter measurements in shrouded and unshrouded radial flow pump impellers,” *Journal of turbomachinery*, vol. 109, p. 71, 1987.
- [40] J. Wu, C. Chen, and S. Wang, “Hydrodynamic effects of a shroud design for a hybrid-driven underwater glider,” *Sea Technology*, vol. 51, no. 6, pp. 45–47, 2010.
- [41] E. Grillos, S. Allison, and B. V. Davis, “Underwater ducted turbine,” Dec. 30 2008. US Patent 7,471,009.
- [42] M. Werle and W. Presz Jr, “New developments in shrouds and augmentors for subsonic propulsion systems,” in *44th AIAA/ASME/SAE/ASEE Joint Propulsion Conference & Exhibit*, p. 4962, 2008.
- [43] G. Lilley and W. Rainbird, “A preliminary report on the design and performance of ducted windmills,” tech. rep., College of Aeronautics Cranfield, 1956.
- [44] B. Gilbert and K. Foreman, “Experiments with a diffuser-augmented model wind turbine,” *Journal of Energy Resources Technology*, vol. 105, no. 1, pp. 46–53, 1983.
- [45] O. Igra, “Research and development for shrouded wind turbines,” *Energy Conversion and Management*, vol. 21, no. 1, pp. 13–48, 1981.
- [46] M. O. L. Hansen, N. N. Sørensen, and R. Flay, “Effect of placing a diffuser around a wind turbine,” *Wind Energy*, vol. 3, no. 4, pp. 207–213, 2000.

- [47] P. M. Jamieson, “Beating betz: energy extraction limits in a constrained flow field,” *Journal of Solar Energy Engineering*, vol. 131, no. 3, p. 031008, 2009.
- [48] G. J. Van Bussel, “The science of making more torque from wind: Diffuser experiments and theory revisited.,” in *Journal of Physics: Conference Series*, vol. 75, p. 012010, IOP Publishing, 2007.
- [49] O. Igra, “Compact shrouds for wind turbines,” *Energy conversion*, vol. 16, no. 4, pp. 149–157, 1977.
- [50] S. McLaren-Gow, P. Jamieson, and J. Graham, “Ducted turbine theory with right angled ducts,” in *Journal of Physics: Conference Series*, vol. 524, p. 012083, IOP Publishing, 2014.
- [51] B. Chen, T. Li, C. Feng, T. Zhang, and D. Zhang, “Concentration for wind power in the built environment,” in *Sustainable Power Generation and Supply, 2009. SUPERGEN’09. International Conference on*, pp. 1–6, IEEE, 2009.
- [52] Y. Su, S. B. Riffat, T. Rogers, H. Zheng, and H. Huang, “A feasibility study of a novel combined solar concentration/wind augmentation system,” *International Journal of Low-Carbon Technologies*, vol. 6, no. 1, pp. 14–21, 2010.
- [53] J. Takeuchi, S. Satake, N. Morley, T. Yokomine, T. Kunugi, and M. Abdou, “Piv measurements of turbulence statistics and near-wall structure of fully developed pipe flow at high reynolds number,” in *Proc. 6th International Symposium on Particle Image Velocimetry*, pp. 21–23, 2005.
- [54] W. Karaki, J. Abboud, N. Daher, M. Osman, and G. Oweis, “Piv measurements in the wake of a cactus shaped cylinder,” in *ASME 2008 International Mechanical Engineering Congress and Exposition*, pp. 2003–2007, American Society of Mechanical Engineers, 2008.
- [55] D. Han and M. Mungal, “Simultaneous measurements of velocity and ch distributions. part 1: jet flames in co-flow,” *combustion and flame*, vol. 132, no. 3, pp. 565–590, 2003.
- [56] C.-K. Choi and D.-K. Kwon, “Wind tunnel blockage effects on aerodynamic behavior of bluff body,” *WIND STRUCT INT J.*, vol. 1, no. 4, pp. 351–364, 1998.
- [57] C. A. Nienaber and K. A. Eagle, “Aortic dissection: new frontiers in diagnosis and management,” *Circulation*, vol. 108, no. 5, pp. 628–635, 2003.

- [58] M. D. Dake, N. Kato, R. S. Mitchell, C. P. Semba, M. K. Razavi, T. Shimono, T. Hirano, K. Takeda, I. Yada, and D. C. Miller, “Endovascular stent-graft placement for the treatment of acute aortic dissection,” *New England Journal of Medicine*, vol. 340, no. 20, pp. 1546–1552, 1999.
- [59] R. R. Baliga, C. A. Nienaber, E. Bossone, J. K. Oh, E. M. Isselbacher, U. Sechtem, R. Fattori, S. V. Raman, and K. A. Eagle, “The role of imaging in aortic dissection and related syndromes,” *JACC: Cardiovascular Imaging*, vol. 7, no. 4, pp. 406–424, 2014.
- [60] T. T. Tsai, M. S. Schlicht, K. Khanafer, J. L. Bull, D. T. Valassis, D. M. Williams, R. Berguer, and K. A. Eagle, “Tear size and location impacts false lumen pressure in an ex vivo model of chronic type b aortic dissection,” *Journal of vascular surgery*, vol. 47, no. 4, pp. 844–851, 2008.
- [61] C. Karmonik, J. Bismuth, M. G. Davies, D. J. Shah, H. K. Younes, and A. B. Lumsden, “A computational fluid dynamics study pre-and post-stent graft placement in an acute type b aortic dissection,” *Vascular and endovascular surgery*, p. 1538574410389342, 2010.
- [62] S. Yu, “Steady and pulsatile flow studies in abdominal aortic aneurysm models using particle image velocimetry,” *International Journal of Heat and Fluid Flow*, vol. 21, no. 1, pp. 74–83, 2000.
- [63] E. Ledneva, S. Karie, V. Launay-Vacher, N. Janus, and G. Deray, “Renal safety of gadolinium-based contrast media in patients with chronic renal insufficiency,” *Radiology*, vol. 250, no. 3, pp. 618–628, 2009.
- [64] C. Saade, R. Bourne, M. Wilkinson, M. Evanoff, and P. Brennan, “A reduced contrast volume acquisition regimen based on cardiovascular dynamics improves visualisation of head and neck vasculature with carotid mdcet angiography,” *European journal of radiology*, vol. 82, no. 2, pp. e64–e69, 2013.
- [65] Z. Cheng, F. Tan, C. Riga, C. Bicknell, M. Hamady, R. Gibbs, N. Wood, and X. Xu, “Analysis of flow patterns in a patient-specific aortic dissection model,” *Journal of biomechanical engineering*, vol. 132, no. 5, p. 051007, 2010.
- [66] C. Karmonik, S. Partovi, M. Müller-Eschner, J. Bismuth, M. G. Davies, D. J. Shah, M. Loebe, D. Böckler, A. B. Lumsden, and H. von Tengg-Kobligk, “Longitudinal computational fluid dynamics study of aneurysmal dilatation in a chronic debakey type iii aortic dissection,” *Journal of vascular surgery*, vol. 56, no. 1, pp. 260–263, 2012.

- [67] C. Karmonik, J. Bismuth, D. Shah, M. Davies, D. Purdy, and A. B. Lumsden, “Computational study of haemodynamic effects of entry-and exit-tear coverage in a debakey type iii aortic dissection: technical report,” *European journal of vascular and endovascular surgery*, vol. 42, no. 2, pp. 172–177, 2011.
- [68] K. M. Tse, P. Chiu, H. P. Lee, and P. Ho, “Investigation of hemodynamics in the development of dissecting aneurysm within patient-specific dissecting aneurismal aortas using computational fluid dynamics (cfd) simulations,” *Journal of biomechanics*, vol. 44, no. 5, pp. 827–836, 2011.
- [69] T. A. Hope, M. Markl, L. Wigström, M. T. Alley, D. C. Miller, and R. J. Herfkens, “Comparison of flow patterns in ascending aortic aneurysms and volunteers using four-dimensional magnetic resonance velocity mapping,” *Journal of Magnetic Resonance Imaging*, vol. 26, no. 6, pp. 1471–1479, 2007.
- [70] W. Thielicke and E. Stamhuis, “Pivlab—towards user-friendly, affordable and accurate digital particle image velocimetry in matlab,” *Journal of Open Research Software*, vol. 2, no. 1, 2014.
- [71] P. A. Rudenick, B. H. Bijmens, D. García-Dorado, and A. Evangelista, “An in vitro phantom study on the influence of tear size and configuration on the hemodynamics of the lumina in chronic type b aortic dissections,” *Journal of vascular surgery*, vol. 57, no. 2, pp. 464–474, 2013.